BETA DECAY HALF-LIVES OF NEUTRON RICH ISOTOPES IN THE GERMANIUM-BROMINE REGION

A Dissertation

Submitted to the Graduate School

of the University of Notre Dame

in Partial Fulfillment of the Requirements

for the Degree of

Doctor of Philosophy

by

Matthew A. Quinn,

_____

Ani Aprahamian, Director

Graduate Program in Physics

Notre Dame, Indiana

April 2010

BETA DECAY HALF-LIVES OF NEUTRON RICH ISOTOPES IN THE GERMANIUM-BROMINE REGION

Abstract

by

Matthew A. Quinn

Understanding the origin of the heaviest elements in the universe is one of the great outstanding problems in physics. More than half of these elements are thought to have been created by a process called the rapid neutron capture, or R process. This process involves many nuclei that are very far from the line of stability. Because these nuclei have such short beta decay half-lives, they are very difficult to produce and study. The vast majority of r-process nuclei have not been observed at all.

This work details the measurement of several r-process nuclei that have never been produced before. These nuclei lie in the r-process path near the $Z = 40$, $N = 60$ region. This region of the chart of the nuclides is also interesting because a rapid change in the shape of nuclei is seen. With the addition or removal of just a few nucleons, nuclei go from a spherical shape to a strongly deformed shape.

For both r-process abundance calculations and nuclear deformation calculations, the beta decay half life and beta-delayed neutron emission ratio P_n values are important parameters. This experiment determined these values for the r-process nuclei in the Germanium-Bromine region. The experimental work was carried out at the National Superconducting Cyclotron Laboratory at Michigan State University.

Twenty-two halflives were determined in our measurments. Three nuclei, ^{90}Se,

^{88}As, and ^{89}As, were measured for the first time. In addition, we have confirmed previously measured half-lives for Y, Sr, Rb, Kr, Br, Se, and As isotopes. The new measurements were used to calculate the P_n values for ${}^{92-90}$Br and ^{96,94}Rb.

An r-process simulation was performed with the results from this measurement. Because of the possible change in shape of the Se nuclei in particular, the uncertainty of r-process production abundances in the $A = 90 - 130$ region are as large as a factor of two. This work determined the shape of the Se isotopes in this region to be deformed, which removed this large uncertainty in the r-process calculations.

CONTENTS

FIGURES

iv

vii

TABLES

CHAPTER 1

NUCLEOSYNTHESIS

1.1   Introduction

Understanding the elements that make up our universe has been a goal of humankind since ancient times. The Greeks gave us the concept of atoms (from the Greek "Atomos" meaning un-cuttable); an idea which states that the universe is made up of some number of elementary particles. This concept remains with us today, and while we know that there are particles more fundamental than atoms, we still can not say why atoms exist in the abundances that we see in nature. The lightest nuclei, including Hydrogen, Helium, and Lithium are thought to have been created shortly after the Big Bang. Therefore, elements heavier than hydrogen and helium must be created inside of stars through thermonuclear reactions [1]. Light nuclei fuse together to create heavier nuclei until a nucleus with maximal binding energy is created. Creation of the heaviest elements however, remains a mystery.

Beyond the Iron region, nuclear fusion is unlikely to occur because of the high electrostatic repulsion between nuclei. This fact seems to indicate that nuclei capturing neutrons create the heaviest elements. Stellar abundance patterns of heavy nuclei suggest that several neutron capture mechanisms may be responsible. Direct evidence of any such mechanisms has been elusive. Models created to reproduce the observed abundance patterns simulate these different processes as a series of neutron captures on seed nuclei. From these models two processes are responsible for

most of the production of heavy nuclei. They are called the rapid (r) and slow (s) neutron capture processes. While a general understanding of the r and s processes has been around for nearly fifty years [1], the sites where they occur still remain unknown. The problem of determining how elements heavier than iron are created remains one of the great unsolved problems in physics [2], and is at the heart of this project.

We try to understand the r-process through simulations. One example includes the ngam code by Bradley Meyer. The ingredients of the code can be divided into astrophysical paramters and nuclear properties. The aim of this dissertation is to measure the evolution of nuclear structure in the region near A=90. This region is thought to be a region for the onset of deformation in nuclear structure. Deformation of a nucleus affects the mass of the nucleus and its beta decay rates. Also, it is a nearly impossible task to measure all or a significant portion of nuclei that may occur along the r-process. We do however aim to measure as far as possible from nuclear stability. The NSCL facility is one such place where we can produce some of these rare r-process nuclei.

This work seeks to measure the beta-decay halflives and beta-delayed neutron emission ratios of new nuclei in the r-process path around the region of yttrium to selenium. These nuclei are interesting because they lie in the r-process path just past a bottle neck in the process at the nucleus ^{78}Ni, which can have a great influence on the abundance peak at $A = 130$ and higher. The nuclei in this region may even be the seed nuclei for the r-process. Their properties may reveal how the r-process starts and how other astrophysical processes end. This work will show the effects of these new halflives on the solar system abundances via an r-process abundance network calculation. In addition to their astrophysical significance, these isotopes are also a few nucleons away from nuclei that exhibit fantastic changes in shape.

The beta-decay halflives of these isotopes will give the first indication of whether additional nuclei also change shape rapidly, and will further the understanding of the mechanisms that govern this and other nuclear properties. This work will explore the effects of these new measurements on the predictions made for nuclear shapes in this region.

1.2 Big Bang

In order to understand how elements are made inside of stars, it is instructive to review how the light elements that make up stars are thought to have been created. The Big Bang is a model used to describe the evolution of the universe from a singularity to its present (and future) state. Monsignor Georges Lemaitre, a physicist and Catholic priest from Belgium, and Russian physicist Alexander Friedmann separately developed theories describing an expanding universe. Lemaitre called the idea a "hypothesis of the primeval atom" [3]. Both Lemaitre and Friedmann's solutions stemmed from the fact that Einstein's general theory of relativity did not permit static solutions for the universe. This meant that instead of being perpetually stable, the universe must have begun at some time in the past. From this initial point, the universe exploded outward and grew into its present enormous size. Two years before Lemaitre's paper, Edwin Hubble had discovered that every other galaxy is receding from our own at a speed proportional to its distance from us [4]. He formulated a relation known as Hubble's Law: $v = H_0 D$ where v is the recessional speed of a particular galaxy, D is its distance from Earth, and H_0 is a constant known as the Hubble constant. That all galaxies in the universe appeared to be moving away from one another seemed to indicate that Big Bang concept was correct.

In 1965 the discovery of the Cosmic Microwave Background radiation gave exper-

imental support for the Big Bang [5] theory. The CMB is a field of radiation, peaked at 160.2GHz, that is seen isotropically throughout the universe. Its existence was predicted as a consequence of energetic photons scattering off of Hydrogen atoms when the universe was only 379,000 years old. After the Big Bang the universe was extremely hot, and took that long to cool enough for Hydrogen atoms to be formed. The presence of the CMB and its extremely isotropic distribution could only be accounted for by the Big Bang hypothesis. The Cosmic Background Explorer (COBE) experiment, begun in 1989, measured the temperature and anisotropy of the CMB with great precision. It revealed that the spectrum of the CMB was described nearly perfectly by a blackbody emitter, as was predicted by the Big Bang theory. In addition to the spectral shape, COBE also revealed slight anisotropies in the CMB distribution throught the universe. This anisotropy in the early universe is believed to be what made it possible for matter condense into galaxies and solar systems instead of being smeared out evenly throughout the universe. These results were seen to be strong enough evidence for the Big Bang hypothesis that the Nobel Prize was awarded to COBE scientists John Mather and George Smoot in 2006.

1.2.1 Big Bang Timeline

The Big Bang theory includes a detailed hypothesis of how the universe evolved from a very short time after it came into existance [6]. In the first instant after the beginning of the universe the four fundamental forces: Gravity, Electromagnetism, Strong and, Weak, were indistinguishable. The universe was extremely hot and dense, and was expanding outward. This time is known as the Planck Epoch, and lasted only 10^{-43} seconds. At this time gravity separated from the other fundamental forces. The universe had cooled enough so that two particles, the X and Y bosons could be created. These theoretical particles could have decayed into two quarks

or one anti-quark and one anti-lepton. Decaying more favorably into two quarks could explain why we see far more matter than anti-matter in the universe today. This period, called the Grand Unification Epoch, lasted until 10^{-36} seconds after the beginning of the universe.

After the Grand Unification Epoch, the universe underwent a rapid expansion. Its size went from approximately 10^{-50} meters in diameter to about 1 meter in diameter. This represents an increase in volume by a factor of 10^{78} in a period of only about 10^{-33} seconds. A scalar field settling into a lower energy state caused inflation. The result of the rapid expansion was that inhomogeneities and anisotropies present in the universe were smoothed out, which is how we observe the universe today. At the end of the Inflation Epoch the universe stopped its rapid expansion, and instead converted the potential energy of the scalar field into radiation and particles such as quarks, electrons, and neutrinos. The universe went from being largely empty to being filled with a hot, dense plasma of particles.

The universe continued to expand and cool and eventually, at a time 10^{-12} seconds after the beginning of the universe, its temperature was cool enough for the electromagnetic and weak forces to decouple. At this time then all of the four fundamental forces existed in the manner in which we observe them today. The universe was still too hot to allow the combination of quarks into heavier particles. It was not until 10^{-6} seconds after the Big Bang that quarks could form heavier particles known as hadrons, which include protons and neutrons. From this time until one second after the Big Bang hadrons dominated the universe, being produced in hadron/anti-hadron pairs until the universe had cooled to the point where these pairs could no longer be created. After that point, the hadrons and anti-hadrons collided and annihilated each other, leaving only a small amount of hadrons remaining. From one second to three minutes after the Big Bang, particles known

as leptons were the dominant matter in the universe. At the three-minute point, Leptons, which include electrons, stopped being produced as particle/anti-particle pairs and began to annihilate each other.

1.2.2 Big Bang Nucleosynthesis

Although at three minutes, the universe was largely made up of radiation, the building blocks of nuclei and atoms are thought to have present. The temperature of the universe had lowered to the point where protons and neutrons could combine to form heavier nuclei, and for only about seventeen minutes light nuclei were created. This process, known as Big Bang Nucleosynthesis or BBN, while creating only a few isotopes, is thought to have been responsible for the production of 98 percent of the nuclei we see today. Protons and neutrons combined to form deuterium, which often captured an additional proton and neutron to form ^{4}He. As can be seen in Figure 1.1, small amounts of deuterium, tritium, ^{3}He, ^{6}Li, and ^{7}Li were created via BBN, while ^{1}H and ^{4}He were dominant. Because ^{8}Be is unstable, the production of heavier elements from ^{4}He must take place through the combination of three ^{4}He nuclei to form ^{12}C. This is called the triple α process, and is known to be extremely slow. Because of the length of time the triple α process takes and because of the small abundances of other isotopes, heavier nuclei were not created in the Big Bang. After only seventeen minutes of activity, the universe had cooled to the point that nuclear fusion was no longer possible. It would not be until 100 million years later that any new nuclei would be created inside the first stars. But it was from the nuclei created in the Big Bang that stars themselves would be created, and would create the elements that we see today.

1.3 Stellar Nucleosynthesis

1.3.1 Charged Particle Nucleosynthesis

A look at the present elemental abundances of our solar system reveals clues about the how those elements were produced in the past, and how they continue to be produced today. Hydrogen and helium are the most abundant, as they were produced in the Big Bang. Elements heavier than H, He, and Li are produced in extremely low abundances. These elements were created only minutes after the Big Bang, over 13 billion years ago. Changes to these abundances are the result of nuclear burning and decay processes inside of stars.

The first stage of nuclear burning consumes hydrogen to create helium. This is done through the $p - p$ chain burning with proton-proton reactions, and through CNO cycle proton reactions on carbon, nitrogen, and oxygen nuclei. The $p-p$ chain converts four protons to one ^{4}He nucleus. The net reaction is:

$$4p + 4e \rightarrow {}^4\text{He}$$
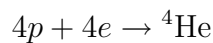
The process must proceed through intermediary reactions though, because the probability of four protons reacting at the same time in a stellar environment is essentially zero. In addition, the reaction:

$$p + p \rightarrow {}^2\text{He}$$
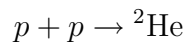
will not occur because the nucleus ^{2}He is unstable. This is also true for reactions that produce ^{3}Li:

$$p + p + p \rightarrow {}^3\text{Li}$$
$$^2\text{He} + p \rightarrow {}^3\text{Li}$$
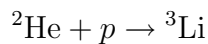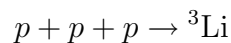
Creating deuterium then, is the solution to converting hydrogen to helium. The reaction:

$$p + p \rightarrow d + e$$
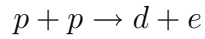
is governed by the weak interaction and is therefore very slow. The mean lifetime for a proton to be converted into deuterium in a stellar environment is about 10^{10} years. This is quite fortunate for us though, as it has allowed our sun to burn long enough for life to develop here on Earth.

Deuterium burning takes place via several reactions, all of which are governed by the strong force and proceed much more quickly than hydrogen burning. The lifetime for a deuterium nucleus in a stellar environment is about 1.6 seconds. The reactions with the largest cross-section are:

$$d + p \rightarrow {}^{3}\text{He} + \gamma$$

$$d + {}^{3}\text{He} \rightarrow {}^{4}\text{He} + p$$
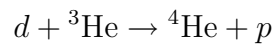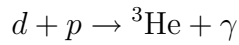
Therefore, burning usually proceeds through the ${}^{3}\text{He}$ nucleus, rather than the

$$d + d \rightarrow {}^{4}\text{He}$$
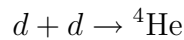
reaction. This cycle is called the $p - pI$ chain. The process can also proceed through the chains:

$$^{3}\text{He} + {}^{4}\text{He} \rightarrow {}^{7}\text{Be}$$

$$^{7}\text{Be} + e \rightarrow {}^{7}\text{Li}$$

$$^{7}\text{Li} + p \rightarrow {}^{4}\text{He} + {}^{4}\text{He}$$

and

$$^{3}\text{He} + {}^{4}\text{He} \rightarrow {}^{7}\text{Be}$$

8

$$^{7}\text{Be} + p \rightarrow {}^{8}\text{B} + \gamma$$

$$^{8}\text{B} + e \rightarrow {}^{8}\text{Be} + \nu$$

$$^{8}\text{Be} \rightarrow {}^{4}\text{He} + {}^{4}\text{He}$$
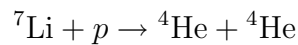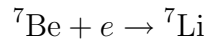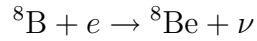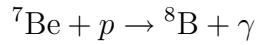
These are known as the $p-pII$ and $p-pIII$ chains, respectively. The $p-pI$ chain is responsible for 86 percent of ^{4}He production, while the $p-pII$ and $p-pIII$ chains are responsible for about 14 and 0.02 percent, respectively.

The energy released in these nuclear reactions opposes the gravitational pressure exerted on the stellar core by the outer layers. When hydrogen burning ceases, the star will contract due to lack of thermonuclear energy release. The pressure on the He in the core will increase until burning is possible. As ^{8}Be is unstable, α-α reactions will not contribute to creating heavier nuclei. Stable ^{12}C will be created by the triple α reaction:

$$3\alpha \rightarrow {}^{12}\text{C}$$
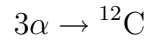
From the carbon nuclei produced in the triple alpha reaction, oxygen and neon are then created through the reactions:

$$^{12}\text{C} + {}^{4}\text{He} \rightarrow {}^{16}\text{O}$$

$$^{16}\text{O} + {}^{4}\text{He} \rightarrow {}^{20}\text{Ne}$$

After helium burning, carbon burning:

$$^{12}\text{C} + {}^{12}\text{C} \rightarrow {}^{20}\text{Ne} + {}^{4}\text{He}$$

$$^{12}\text{C} + {}^{12}\text{C} \rightarrow {}^{23}\text{Na} + p$$

$$^{12}\text{C} + {}^{12}\text{C} \rightarrow {}^{23}\text{Mg} + n$$
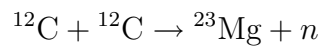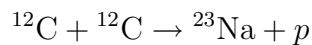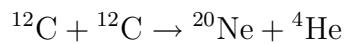
neon burning, and oxygen burning occur. The final stage of charged particle reactions is silicon burning. Because of silicon's high Coulomb barrier, direct burning

9

(^{28}Si + ^{28}Si) does not take place. Instead, as the temperature inside the star increases, nuclei are photodisintegrated by the high energy gamma rays present. The result is that ^{28}Si and ^{4}He nuclei are available to interact and create ^{32}S. ^{32}S will capture ^{4}He and form ^{36}Ar and so forth, allowing the star to build up heavier and heavier elements. Charged particle reactions continue until ^{56}Fe is created, which has a higher binding energy per nucleon than heavier nuclei. This means that further charged particle reactions are unlikely to occur. In order to create heavier elements, neutron captures will be the dominant mechanism. The two neutron capture processes responsible for most of the heavy element production are called the s- (slow) and r- (rapid) neutron capture processes.

In addition to the s- and r- processes, there are other processes that contribute to the total heavy element production [1]. This was realized because there are proton-rich nuclei such as ^{190}Pt or ^{168}Yb that cannot be created by the neutron-rich r- and s-processes. The p- (proton capture) process creates heavy proton-rich nuclei by a series of γ-n or γ-α reactions on heavy seed nuclei. Thus, the p-process is not responsible for creating heavy elements from lighter constituents as in charged particle reactions or the s- and r-processes, but it does change the observed heavy element abundances. Because of the high temperatures necessary for the photodisassociations, possible sites for the p-process include neutron star mergers and supernova shock fronts [8]. The rp- (rapid proton capture) process does create heavy nuclei from lighter seeds. It entails making heavy proton rich nuclei through a series of proton captures on proton-rich seed nuclei followed by β^+ decays. Sites for the rp-process are thought to include X-ray bursts on accreting neutron stars and nova explosions of white dwarfs.

The results of Big Bang and stellar nucleosynthesis can be seen in the elemental abundances present inside of our own sun. Nuclei created in the Big Bang and

in older generations of stars are still present today. Figure 1.2 shows these abundances. It is important to note that these abundances show the effects of nuclear structure. Especially stable nuclei like ^{4}He, ^{12}C, ^{16}O, and ^{56}Fe are produced in large abundances. In addition the r- and s-process peaks occur at the points where these processes encounter closed neutron shells. Therefore, in order to understand the abundances of the elements, we must understand the nuclear structure that guides their creation.

1.3.2 S Process

The first process that dominates production of elements heavier than iron is the slow neutron capture process (s-process)[9]. The s-process is characterized by lower neutron fluxes (compared to the r-process) and a path close to stability. For a stable or slightly unstable nucleus of charge Z and mass A, the capture of a neutron can lead to a stable or an unstable (A+1) nucleus. If the product nucleus is stable, it will simply wait to capture an additional neutron (or neutrons) before undergoing beta decay. If the product nucleus is unstable, it may beta decay to its Z+1 isobar, or it may capture another neutron before beta decay has a chance to occur. The neutron flux, beta decay half-lives and neutron capture cross sections determine how long the process takes, where nuclei will be involved, and what the final abundances will be. The observed solar abundances show large peaks at masses 90, 135, and 210. These are related to where the s-process path intersects the N = 50, 82, and 126 shell closures.

The s-process can be modeled using a series of coupled differential equations, which produce time dependent isotopic abundances.

$$\frac{dN_A(t)}{dt} = N_n(t)N_{A-1}(t)\langle\sigma\nu\rangle_{A-1} - N_n(t)N_A(t)\langle\sigma\nu\rangle_A - \lambda_{\beta(A)}N_A(t)$$

The first term on the right side of the equation describes its production by neutron capture on the lighter A-1 nucleus. The second term describes its destruction by capturing a neutron to form the A+1 nucleus. The third term describes its destruction by beta decay. With low capture cross sections and a large enough neutron flux a steady flow will be achieved, with $N_A \times \langle \sigma v \rangle_A = const$. The system of equations can then be solved analytically by making the following substitutions [6]:

$$\lambda_n = 1/t_{n\gamma} = N_n \langle \sigma v \rangle_A.$$

One of the following assumptions must be made then: either $\lambda_1 \ll \lambda_2$ or $\lambda_1 \gg \lambda_2$. For the best fit to the data multiple exponential neutron exposures are needed.

This model breaks down for cases where $\lambda_1 = \lambda_2$. These are the so called s-process branching points which include ^{134}Cs, ^{148}Pm, ^{151}Sm, ^{154}Eu, ^{170}Yb , and ^{176}Lu. A network using the temperature dependent beta decay and neutron capture rates must be used at these points.

Three different components of the s-process have been recognized, in order to correctly reproduce the solar system s-process abundances. The first is the Main component. It is responsible for producing most of the nuclei with A 90-208. It takes place in the He burning shells in low mass ($< 4 M_\odot$) asymptotic giant branch (AGB) stars. The neutron source comes from ^{13}C "pockets" created in the H-He intershell. Recurrent thermal instabilities above the He burning shell cause the H-He intershell to become convective during the thermal pulse. Pockets of ^{13}C are created in the intershell by protons injected from the hydrogen envelope during each Third Dredge Up (TDU) phase capturing on ^{12}C. After the thermal pulse, convection mixes the He, C and s-process material. The ^{13}C + $\alpha \rightarrow {}^{16}$O + n reaction then produces the neutrons required for the s-process at a temperature of T $\sim 3 \times 10^8$ and a flux of

$n_n = 10^8 cm^3$ for a period of about 20000yr.

The second component of the s-process is the weak component. It produces nuclei with mass up to A $\sim$ 90 and is thought to occur in massive stars. The primary neutron source is the ^{22}Ne $+ \alpha \rightarrow ^{25}$Mg $+ n$ reaction. This occurs in regions of convective He burning. ^{22}Ne is produced from the conversion of CNO material into ^{14}N in the H burning shell. Thus this process is metallicity dependent. The ^{14}N then captures two alpha nuclei in He region to produce ^{22}Ne.

The third component is the strong component introduced by Clayton and Rassback in 1967. It is responsible for producing of the ^{208}Pb abundance, and occurs in low metallicity Fe/H < -1.5 low mass AGB stars.

These predictions of s-process abundances are bolstered by experimental evidence from grains of stardust found in meteors. These grains contain s-process elemental abundances that agree closely with predicted s-process abundances [?] [?] [?]. The large difference in abundances of these isotopes as compared to those in our solar system is taken as evidence that these grains really do come from outside the solar system. This material may be reliably called s-process material, and indicates that the s-process abundance predictions are largely reliable. Having reliable s-process abundnace predictions is important because, as will be described below, the r-process abundances that this project and other works depend upon will be derived using s-process abundnace predictions.

1.3.3 R Process

The abundance peaks at masses 80,130, and 190 must be produced by a process separate from the s-process. The intersection of these masses with the closed neutron shells indicates that the nuclei involved in this process are much farther from stability than the s-process nuclei. Because of this, the r- or rapid neutron capture process is

defined by beta-decay lifetimes that are longer than the time necessary to capture a neutron. This is in contrast to the s-process, which is characterized by beta-decay lifetimes that are much shorter than the neutron capture times. A path far from stability with lifetimes ~ 100ms necessitates a large flux of neutrons, which suggests that the r-process occurs in explosive environments such as supernovae.

Burbidge, Burbidge, Fowler and Hoyle (B2FH) in 1957 theorized that the solar abundances of the elements can be explained via a number of different processes, however the astrophysical conditions and sites where an r-process may take plance are still unknown [1]. Their paper describes how the double peaks seen in abundance plots are due to the superposition of slow and rapid neutron capture processes. It also shows how these peaks are due to the neutron shell closures that each process path encounters. They were able to make calculations for the abundances from these processes, and were able to estimate timescales for the process as well. These classical models used ^{56}Fe as a seed for the r-process. Newer models attempt to take into account the physics of the proposed site in a more realistic way. For models using core-collapse supernova as the site of the r-process, the tremendous amount of energy released by the collapse (10^{56}ergs) is enough to disassociate the nuclei in the core into protons and neutrons. As the temperature drops, the protons and neutrons combine to form alpha particles. Because of the high density, electrons in the area are degenerate, and it becomes energetically favorable for protons to capture electrons and form neutrons. Alpha particles fuse together to form heavier nuclei, and in the presence of excess neutrons, can form neutron rich nuclei heavier than iron. This scenario is called an "alpha rich" freezeout, and provides seeds for the r-process in a more realistic way than the classical model.

1.3.4 R Process Abundance Observations

Determining the amount of r-process material present in a particular star is not a trivial matter. The elemental abundances present in a given star include material created in BBN as well as nucleosynthesis from previous generations of stars. Therefore the presently observed abundances are a superposition of possibly many p-, s-, and r-processes. For the elements heavier than iron, the solar system r-process abundances must be obtained from the modeled s-process abundances. As the s-process path occurs close to the line of stability, beta-decay rates and neutron capture cross sections can be measured for these nuclei. With this data and information about the stellar environment, it is possible to generate the solar abundance due to s-process nuclei. The r-process abundance is then taken as the difference between the solar observed abundances and the s-process abundances.[10]

$$Rprocess = Solar - Sprocess$$

The uncertainties in the r-process abundances due to uncertainties in observations and s-process calculations have been treated by [11]. The resulting error bars are small for r-process only elements such as Ba and Ir, while being larger for the elements created mainly in the s-process.

Recent observations of very old galactic halo stars have shed new light onto the r-process, while creating new questions at the same time[12]. A class of stars called Metal-poor halo stars show remarkable agreement with solar system r-process abundances. These stars are called metal poor because they contain less iron relative to hydrogen than our sun. Although in astronomy any element past helium can be referred to as a metal, iron is used to classify the metallicity of stars because it is produced in high abundance and can easily be detected through spectroscopy. The log of the ratio of iron to hydrogen is generally referred to when determining

metallicity. Stars with values of less than one are considered metal poor ($\log Fe/H <$ -1).

Halo stars are thought to contain the remnants from only one or a few r-processes. This is because they are very old and contain very little heavy element abundance. These halo stars were produced from the remnants of the first stars in the galaxy and would contain r-process material only from the nearby stars of that first generation. Thus, unlike the solar abundances, they contain very pure r-process contributions instead of a superposition of multiple r-process events from multiple generations of stars.

For a number of different stars spanning a wide range of metallicities, the r-process abundances of elements with $Z > 55$ agree nicely with the solar system abundances [13]. This suggests that the mechanism for creating the r-process elements above $Z = 55$ is quite robust, and does not differ very much from event to event. However for elements with $Z < 55$, there is a large under-production of r-process elements in the halo stars. It is unclear then if the r-process outputs can differ for different stellar conditions, or if there are two (or three) different types of r-processes that occur with different temperature and neutron density conditions. Suggestions of a weak r-process [15] or of a Light Element Primary Process [14] have been made in order to describe these abundance patterns. It is clear, though, that because Ge-Br isotopes are at the center of this disputed region, measuring their nuclear properties is critical to understanding the differences between metal-poor and solar heavy element abundances.

1.3.5   R Process Models

Because the nuclei involved in the r-process are so far from stability, measurements of even their most basic properties has been rare. Early models of the r-

process [17] [1] [16] set up a system of differential equations that describe the change in isotopic abundances. In general this includes neutron captures, beta-decays, beta-delayed neutron emission, photodisassociation, and fission for all nuclei involved in the process.

This system of equations is greatly simplified if one assumes that the abundance of each isotopic chain is contained largely in one nucleus. This is because the neutron captures in an isotopic chain will occur before any of the nuclei will have a chance to beta-decay. As more and more neutrons are added the last neutron will be less strongly bound to the nucleus. At some point the gamma rays present in this (presumably) violent scenario will photodisassociate the last neutron added, preventing further neutron captures. The nucleus will then wait at a particular mass until it beta-decays to the next isotope. This "waiting point" nucleus contains the majority of the matter abundance for its isotopic chain. The waiting points are determined by the temperature of the scenario and the binding energy of the last neutron, which can be obtained from the nuclear mass. The series of differential equations describing the r-process can then be simplified greatly, using only the abundance for each isotopic chain. The dependence on the neutron capture rates is also removed, meaning that the simulation will rely only on the beta-decay rates, nuclear masses, neutron density, and temperature. The equation for the abundance of each isotopic chain is given by:

$$\frac{Y(Z, A+1)}{Y(Z, A)} = n_n \frac{G(Z, A+1)}{2G(Z, A)} \left(\frac{A+1}{A}\right)^{3/2} \left(\frac{2\pi h^2}{m_u kT}\right)^{3/2} e^{\left(\frac{S_n(Z, A+1)}{kT}\right)}.$$

Where Y(Z,A) is the abundance of the nucleus ^{A}Z, $Y(Z, A+1)$ is the abundance of the nucleus $^{A+1}$Z, $G(Z, A)$ and $G(Z, A+1)$ are the partition functions for ^{A}Z and $^{A+1}$Z, n_n is the neutron number density, S_n is the neutron separation energy, and T is the temperature. [19] and [18] showed what neutron density and temperature

17

range the waiting point approximation is valid for, and that this region successfully reproduces the observed r-process abundances. Generally, temperatures higher than 1GK and neutron densities larger than $10^{20}/cm^3$ are required to successfully reproduce the r-process.

1.3.6 R Process Sites

The location of the r-process is currently unknown. From an early time [1] it was recognized that explosive scenarios such as core collapse supernova or neutron star mergers were good candidates for the site of the r-process. This is because of the need for high neutron number densities ($> 10^{20}$) and high temperatures ($> 1GK$). Core collapse supernova start out as massive stars ($M = 8 - 100\ M\odot$). Through nuclear burning they reach a point where their cores are composed of iron group nuclei. Because the iron group nuclei have the highest binding energy per nucleon further charged particle reactions will be endothermic. The core stops burning and can no longer support the gravitational pressure from upper layers of the star, which causes the core to collapse. As the temperature in the core increases, nuclei are photo-disintegrated to alpha particles and bare nucleons. The density of the core increases until it reaches nuclear density and a proto-neutron star is formed. A shock wave rebounds from the now incompressible core and is sent out through the outer layers of the star.

Unfortunately, in models of the explosion, this shock stalls in the outer layers of the star and does not produce an explosion that would transfer material throughout the interstellar medium. Energy released by the proto-neutron star in the form of neutrinos might be a solution to this shock stall, but the amount of energy deposited by these neutrinos is still not enough to trigger an explosion. Further attempts in the form of two- and three- dimensional simulations, with the inclusion of magnetic,

18

acoustic, convective, rotational, and asymmetric effects have been made with no definitive explanation emerging.

Perhaps the most promising explanation has been the neutrino-driven wind scenario. In it, neutrinos from the cooling center of the proto-neutron star deposit energy into its surface and ablate material.[20] [21] This high entropy ($S > 400$kb), neutron rich material, called the neutrino driven wind, is driven from the proto-neutron star into the low density region behind the shock. There it recombines mainly through alpha captures to form neutron rich seed material heavier than iron. The r-process then occurs with these neutron rich seeds instead of iron group nuclei, as in the canonical r-process models.

CHAPTER 2

NUCLEAR STRUCTURE

2.1 Structure

The goal of nuclear physics is to understand the properties of a nucleus as a function of the number of protons and neutrons that make it up. Since the 1940's the shell model has been accepted as way to successfully describe the properties of a nucleus[22]. Its largest success has been the description of the so called magic numbers. These are the numbers of protons and neutrons for which exciting a particle to the next excited state takes a large amount of energy. Starting with a description of a single bound nucleon in a simple square well potential is a natural first step. It is a mathematically simple description of a central potential that gives a bound solution with a non-zero ground state energy, and a series of excited states with large energy gaps between certain numbers of nucleons. These energy states are generated by solving for the eigenvalues of the Schrodinger equation, using the square well potential in the Hamiltonian. The levels are filled in order due to the Pauli principle, which says that two nucleons can not have the same quantum numbers[23]. Unfortunately, the magic numbers produced are not the same as seen in experiments, and the energy gaps are identical in energy also unlike what is seen in experiments. The magic numbers 2,8,16,20,28,50,82, and 126 were able to be described using a harmonic oscillator plus a term proportional to the square of the orbital angular momentum and a term proportional to the orbital angular

momentum dotted with the spin.

Figure 2.1. Shell model level scheme. [22]

Even though the correct magic numbers are predicted by the shell model, it is important to note that this is not the full story. The spacing and ordering of the orbital levels changes as nucleons are added to a system. This is obvious from the fact that the potential will change with the addition of a proton or neutron. In addition to the change in the central potential, nucleons also have interactions with other nucleons. These interactions depend on the overlap of the individual nucleon orbits and their energy spacing. These interactions include not only proton-proton and neutron-neutron interactions, but proton-neutron interactions as well. In fact, the p-n interactions are largely responsible for the changes in the shape of a nucleus, known as nuclear deformation.

Further from stability the shell structure can change a great deal. Evidence for

the breakdown of the N $= 8$ shell gap has been seen near the neutron drip line in ^{12}Be [24]. The emergence of a gap at N $= 14$ in ^{22}O has also been seen. Some predictions have suggested that for heavier nuclei, the familiar magic numbers will be quenched far from stability and new magic numbers will appear, while others indicate that the old magic numbers will remain. Using r-process simulations some have shown that a quenching of the N=50,82 gaps is necessary to correctly reproduce the observed solar system r-process abundances[25]. Experiments in the ^{132}Sn region have shown some evidence for this effect[27], but there is still no conclusive picture. Determining the role of shell closures and magic numbers in the neutron rich region is extremely important for nuclear structure and nuclear astrophysics. New magic numbers or the quenching of shell effects test our understanding of the nucleus and will change the nuclear physics inputs for the r-process.
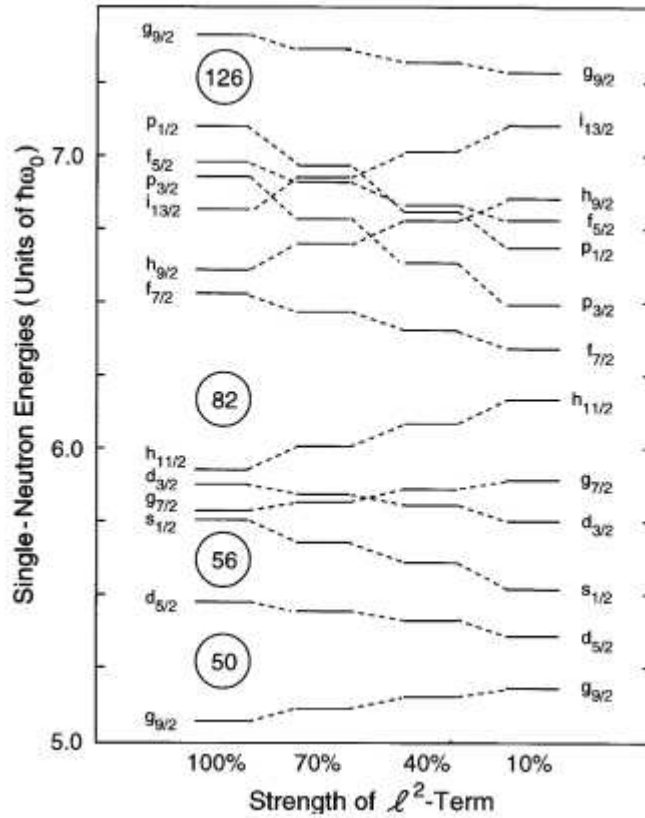
Figure 2.2. Nilsson-model calculation showing evolution of single neutron energy levels as l^2 term is decreased. Decreasing this term in the modified harmonic oscillator Hamiltonian represents more neutron rich nuclei, therefore the plot shows the evolution of shell structure as nuclei become more neutron rich. The N = 50, 82, and 126 shell gaps are all reduced in this calculation because the low j states above the shell gaps are reduced in energy, while the high j state below the gaps are raised in energy.

2.1.1 Vibrational Nuclei

As the number of valence nucleons increases, the number of residual p-n inter-actions increases[28][23]. This increased number of residual p-n interactions can overwhelm the single particle shell model structure. The mixing of many nearly degenerate levels produces one lowered level with a highly coherent wave function. Such a state will have collective properties for the entire nucleus. Expanding the residual interaction into multipoles will give monopole, dipole, quadrapole, and higher terms. The electric quadrapole term plays a strong role in the low lying states of a nucleus. A quadrapole excitation of a spherical nucleus will cause the nucleus to oscillate in shape. The situation can be understood by treating the nu-cleus as a liquid drop and describing the shape of the nucleus with a deformation on the spherical shape[7].

$$R = R_0[1 + \Sigma_\mu \alpha_\mu \cdot Y_{2\mu}(\Theta, \phi)].$$

The Hamiltonian is then:

$$H = \frac{1}{2}C_\lambda \Sigma_\mu |\alpha_{\lambda\mu}|^2 + \frac{1}{2}D_\lambda \Sigma_\mu \left|\frac{d\alpha_{\lambda\mu}}{dt}\right|^2$$

where C_λ is a parameter related to the surface and Coulomb energies of the nuclear liquid drop, and $D_\lambda = \frac{\rho R_0{}^5}{\lambda}$. C_λ and D_λ are related by $\omega_\lambda = \left(\frac{C_\lambda}{D_\lambda}\right)^{1/2}$, and $\hbar\omega_\lambda$ is the quantum of vibrational energy for the multipole λ.

One phonon quadrapole excitation of a 0^+ ground state in an even-even nucleus will produce a 2^+ excited state. A second phonon can produce a triplet of states with $J^\pi = 0^+$, 2^+, or 4^+. The two phonon triplet states should be at roughly twice the energy of the one phonon state. The ratio E_4^+/E_2^+ or the ratio of the energy of the first 4^+ level to the energy of the first 2^+ level is used as a guide

to identify vibrational collective nuclei. In addition to this vibrational structure, enhanced collectivity will also lower the first 2^+ state in relation to its position in a closed-shell nucleus. Thus the energy of the first 2^+ state can be used as a check for increasing or decreasing collectivity in a series of isotopes.

2.1.2 Deformed Nuclei

The addition of more nucleons to a nucleus already between shell closures will produce more residual p-n interactions. These interactions will result in more configuration mixing, and a further departure from a spherical shape. Eventually even the multipole vibrations will not be able to accurately describe the system, and a new formalism is needed. These nuclei are seen as having a permanent deformed shape in the ground state and excited states. Deformed nuclei can have quadrapole and higher deformations, with the quadrapole being the most common at low energies. The shape of a nucleus can then be described by the equation[7]:

$$R = R_0[1 + \Sigma_\mu \alpha_\mu \cdot Y_{2\mu}(\Theta, \phi)].$$

Nuclei can either be prolate shaped (football) or oblate shaped (frisbee). Because the deformed shape breaks angular symmetry the nucleus will be free to rotate. The rotational Hamiltonian is:

$$H = \frac{\hbar^2}{2I} J^2.$$

where I is the moment of inertia, and J is the rotational angular momentum operator. Generally, I can be obtained by expanding the equation

$$I = \frac{\hbar^2}{2} \left(\frac{\partial H}{\partial J(J+1)} \right)^2$$

25

in powers of $J(J+1)$. For the simple case of considering the nucleus a rigid ellipsoid, this becomes:

$$I = \frac{2}{5}MR_0^2(1 + 0.31\beta)$$

where $\beta = \frac{4}{3}\sqrt{\frac{\pi}{5}}\frac{\Delta R}{R_{av}}$

For the ground and low-lying states in even-even nuclei all of the angular momentum will be due to rotation. The expression for the energies of these states is then:

$$E = \frac{h^2}{2I}J(J+1).$$

The first few excited states will have energies of:

$$E_2^+ = \frac{6h^2}{2I}$$

$$E_4^+ = \frac{20h^2}{2I}$$

$$E_6^+ = \frac{42h^2}{2I}$$

Therefore, the ratio E_4/E_2 will be $20/6 = 3.33$. We can get an approximate idea of the behavior of a nucleus by looking at its E_4/E_2 ratio.

Spherical: < 2

Vibrational: 2

Rotational: 3.33

Because the deformation is a result of collective behavior, the first 2^+ will also be lowered compared to spherical nuclei.

2.1.3 $N_p N_n$ Scheme

A useful way to study collectivity and deformation is through a parameterization of the valence proton-neutron interactions. This is called the $N_p N_n$ scheme because it looks at the product of the number valence protons and neutrons[30]. It is assumed that the onset of collectivity and deformation is due solely to the proton-neutron interactions. The product of the number of protons and neutrons (or holes) counted from the nearest closed shell is plotted versus the E_2^+ or E_4^+/E_2^+ values for a series of nuclei. These plots can show trends across regions that give important clues to changes in the nuclear structure.

Looking at the average number of proton-neutron interactions per valence nucleon can give good rules of thumb concerning the general nuclear structure. This is called the "promiscuity factor" and is given by:

$$P = N_p N_n / N_p + N_n.$$

Plotting the E_4^+/E_2^+ ratio versus P shows us that nuclei are deformed ($E_4^+/E_2^+ = 3.33$) for $P > 5$, and may be deformed for $P = 4$. This means that for a nucleus to be deformed, both N_p and N_n must be greater than or equal to 4.

2.1.4 Structure $A = 100$

The reordering of levels can have consequences for the ground state properties as well. Nuclei in the $A = 100$, $N = 60$ region show a sudden and severe change in the ground state E_2^+ levels, E_4^+/E_2^+ ratios, quadrapole deformations, and half-lives. This behavior is unlike the gradual change from spherical to vibrational to deformed properties. The presence of two configurations, one spherical, one deformed account for the different properties of the nuclei in this region.

A suggested explanation for this behavior is the monopole component of the

proton-neutron interaction[31]. The monopole component of the proton-neutron interaction does not depend on the angle between the proton and neutron orbits (as the $P_0(\cos\theta)$ Legendre polynomial has no θ dependence). It does depend on the radial distance between the proton and neutron orbits, so that the proton-neutron interaction will be strong for orbits with the same orbital angular momentum regardless of what their total angular momentum is. So for instance, the $\nu 1g_{7/2}$ (and $\nu 1h_{11/2}$) orbit and the $\nu 1g_{9/2}$ orbit will have a strong proton-neutron interaction, which will have the effect of lowering the orbits. As the $\nu 1g_{7/2}$ (or $\nu 1h_{11/2}$) neutron orbit is filled and the $1g_{9/2}$ proton orbit is lowered, the the shell gap at $Z = 40$ will be reduced or destroyed.

If the nucleons fill the reordered shells from the bottom up as usual, the nucleus will be spherical. However, if a pair of protons from the $2p_{1/2}$ orbit is excited across the reduced shell gap a deformed configuration will result. This is because the excitation of a proton pair creates more valence protons, which increase the collectivity of the system. In the P scheme this would correspond to configurations in ^{100}Zr with $N_p = P = 0$ for a strong $Z = 40$ shell gap, and $N_p = 10, P > 4$ for no shell gap.

Deformed "intruder states" have been seen in other regions of the nuclear landscape [32]. In such regions near proton shell closures, the lowest state of the deformed configuration is a 0^+ level that is seen to lower in energy as neutrons are added toward mid-shell. The 0^+ state is lowest in energy at the middle of the neutron shell, and increases in energy as neutrons are added past the middle of the shell. The difference for nuclei in the $A = 100$ region is that the deformed 0^+ state is lowered beneath the 0^+ spherical ground state. Thus the ground state becomes deformed, and the ground state properties change dramatically.

The rapid transition to deformed ground states has been seen in Mo isotopes

above the $Z = 40$ shell closure at Zr, and Sr isotopes below. Models predict strong deformation in the Kr and Se isotopes in this region [45], but measurements of Kr isotopes do not indicate strong deformation [33]. Because the beta-decay rates depend on the ground state deformations, measuring the beta-decay half-lives of nuclei in this region will help to indicate if the nuclei below Zr and Kr around $A = 100$ also have sudden transitions to deformed ground states.
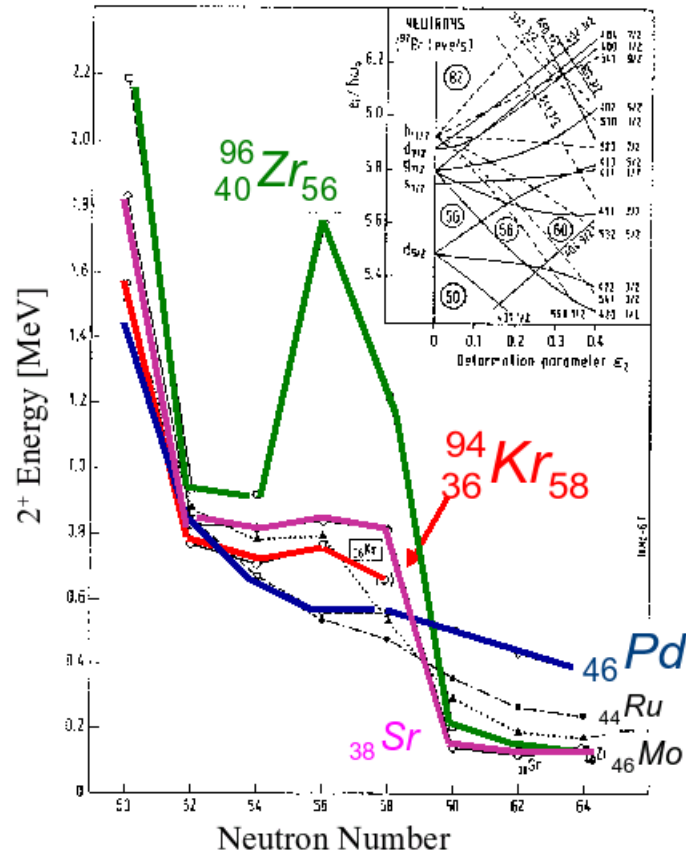
Figure 2.3. First 2^+ energy levels in neutron rich nuclei around $A = 100$. A rapid drop in energy is seen between $N = 56$ and $N = 60$. This drop corresponds to the rapid onset in deformation due to the presence of intruder states.
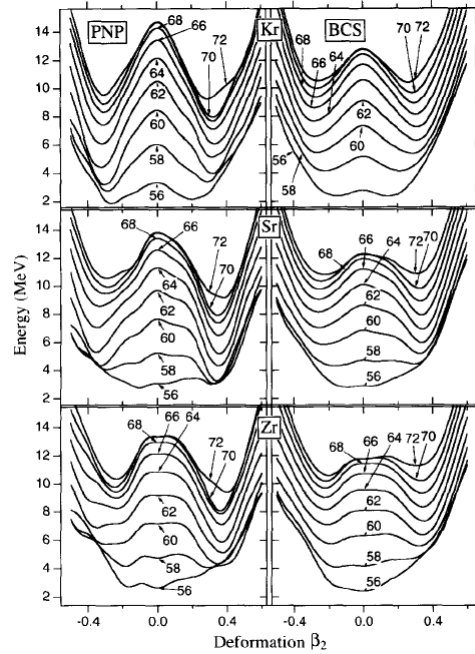
Figure 2.4. Calculation of ground state energy as a function of deformation for neutron rich Kr, Sr, and Zr isotopes. The onset of a deformed minimum for N = 60 in the Zr isotopes can be seen, while deformed ground states are predicted below N = 60 for the Sr and Kr isotopes. This suggests that deformation may be seen in the Se and Ge isotopes with N < 60. From [45]
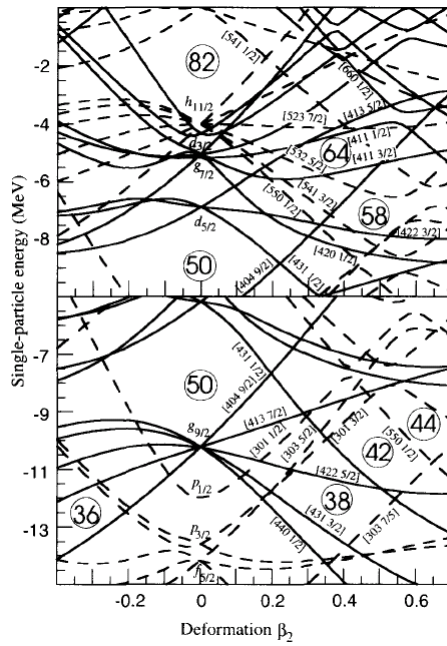
Figure 2.5. Wood Saxon single particle neutron (top) and proton (bottom) energy levels as a function of deformation parameter β. From [45].

31

2.2 Nuclear Physics Inputs for R-Process Simulations

2.2.1 R-Process Codes

R-process simulations are done by solving a network of coupled differential equations for the abundances of each isotope. These equations can include terms for neutron captures, beta-decays, beta-delayed neutron captures, photodisintrigations, neutrino captures, and fission. The network solves for the abundance of each isotope given initial choices of parameters such as: seed nuclei, neutron number density, temperature, and duration of the simulation. In classical r-process models ^{56}Fe is chosen as a seed, while simulations of an alpha-rich freezeout use multiple neutron-rich seed nuclei. The neutron rich nuclei in the Ge-Br region of interest in this work are among these seed nuclei. For a canonical r-process simulation considering neutron capture, beta decay, and beta-delayed neutron emissions each differential equation will look like [?]:

$$\dot{Y}(Z, A) = \sum_{Z',A'} \lambda_{Z',A'} Y(Z', A') + \sum_{Z',A'} n_n \langle \sigma \nu \rangle_{Z',A'} Y(Z', A') Y_n$$

Where $Y(Z, A)$ is the abundance of the nucleus ^{A}Z, σ is the neutron capture rate for the nucleus ^{A}Z-1. The first term on the right hand side of the equation includes beta-decays and photodisassociations, while the second term includes neutron induced reactions.

For large enough neutron number densities and high temperatures (i.e. photon densities), neutron capture and photodisassociation will occur much more quickly than beta decay. This situation is known as an $(n, \gamma) \Leftrightarrow (\gamma, n)$ equilibrium, where the nucleus with the maximum abundance for each isotopic chain must wait for the slower beta decay before proceeding to the next isotopic chain. The change in abundance will then look like:

$$\dot{Y}(Z, A) = \lambda_{A+1} Y(Z, A + 1) - \langle \sigma \nu \rangle_{Z,A} Y(Z', A') Y_n$$

An equilibrium condition ensures that $\dot{Y}(Z,A) = 0$ The reaction rates λ between neutron capture and photodisassociation are related by detailed balance, and are given by :

$$\lambda_{A+1} = \left(\frac{2G(Z,A)}{G(Z,A+1)}\right)\left(\frac{A}{(A+1)}\right)^{3/2}\left(\frac{m_u kT}{2\pi h^2}\right)^{3/2}\langle\sigma v\rangle_A e^{\left(\frac{S_n(Z,A+1)}{kT}\right)}.$$

where G is the partition function, T is the temperature, and S_n is the neutron separation energy for the nucleus $^{A+1}$Z. Thus, the location of the waiting point nuclei depends largely on the nuclear mass (via the S_n), and the temperature. Combining the abundance equation and rate equation above, the abundance ratios for each mass of a given Z can then be calculated from the equation:

$$\frac{Y(Z,A+1)}{Y(Z,A)} = n_n \frac{G(Z,A+1)}{2G(Z,A)}\left(\frac{A+1}{A}\right)^{3/2}\left(\frac{2\pi h^2}{m_u kT}\right)^{3/2}e^{\left(\frac{-S_n(Z,A+1)}{kT}\right)}.$$

In dynamic network codes, for a given time step abundances are calculated in addition to new values of n_n and T. The simulation is ended when the neutron number density or temperature drop below a certain level. Static network codes calculate abundances the abundances in each isotopic chain for the full simulation time, then factor in the contribution to each abundance due to beta decays. The most important nuclear physics inputs then are the nuclear masses (Sn values), beta-decay halflives, and the beta-delayed neutron emission ratios. For nuclei far from stability these values are unknown and must be calculated. There are often large differences in predicted values, so it is critical that these properties be measured. Because the astrophysics surrounding the location and mechanism for the r-process are unknown, accurate nuclear physics information can help to constrain the astrophysical parameters.

2.2.2 Masses

Because so few r-process nuclei have been measured, performing r-process simulations requires the use of predictions for nuclear properties. Nuclear masses are

perhaps the most important nuclear data needed for r-process calculations. Masses determine the neutron separation energies, Q values for beta decays, and define the neutron drip line. With the temperature, the nuclear masses dictate what the r-process path will be. For a given temperature of $1 - 2 \times 10^9 K$, the r-process waiting points will occur at nuclei with a S_n of 1.4MeV. Because very few masses have been measured for r-process nuclei, abundance calculations rely heavily on nuclear mass extrapolations or calculations.

The first mass model was the semiemperical model from von Weizsacker [34] and Bethe and Bacher [35], which treated the nucleus as liquid drop. It contains terms for nuclear volume, volume symmetry, surface energy, and coulomb energy in addition to a surface symmetry term added by Meyers and Swiatecki [36]. Four coefficients (all terms except Coulomb) are then adjusted to fit the measured mass values and create a formula to predict unknown masses. This formula produces a surprisingly good fit for only five terms with an overall rms deviation of 2.97MeV [37], but fails badly for closed shell nuclei, with an error of around 10MeV.
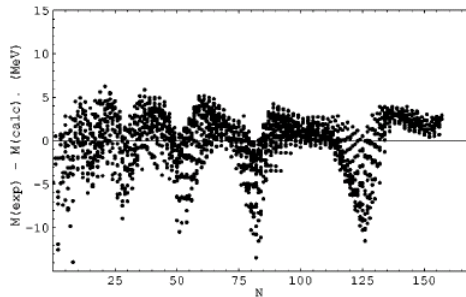
Figure 2.6. Difference between nuclear mass from the Semi-empirical mass model and experimentally measured nuclear masses as a function of neutron number. The overall RMS fit is good, but large deviations at N = 28, 50, 82, and 126 can be seen. From [37].

Improved mass models attempted to introduce microscopic shell corrections to

the liquid drop model. These macroscopic-microscopic models include the Finite Range Droplet Model (FRDM) and the Extended Thomas Fermi plus Stutinski Intergral (ETFSI) formulas. The FRDM [38] differs from earlier liquid drop models in that it takes into account the effect on the surface energy due to the finite range of the nucleon-nucleon interaction. It also treats the effect of nuclear shape on the Coulomb field and the diffuseness of the charge distribution, and introduces a exponential compressibility term that corrects earlier drop models' tendencies to overstate the central nuclear density. The microscopic corrections include a potential for use in the Strutinsky integral in order to introduce shell effects into the calculation. It is composed of three parts: a spin independent nuclear part, a spin orbit part and a Coulomb part.

The FRDM also uses a version of the BCS treatment for paring corrections, a Wigner term to treat $T = 0$ pairing in nuclei with $N \approx Z$, and a charge-asymmetry term to account for the energy difference between mirror nuclei. The results for the FRDM are much improved over earlier liquid-drop models, as it produces a rms error of 0.67MeV and shows shell effects.

The ETFSI mass formula [39] is based on the extended Thomas Fermi approximation. Both the macroscopic and microscopic parts of the calculation center around a Skyrme-type force. This means that unlike the FRDM calculations, the microscopic and macroscopic parts of the calculation are done self-consistently. The results from ETFSI calculation are similar to the purely microscopic Hartree-Fock calculations, while being much faster to perform.

The latest mass formulas treat the nucleus microscopically, in that they attempt to solve the Schrodinger equation for some choice of nuclear mean-field force. The Hartree Fock formula solves the Schrodinger equation for an initial choice of the mean field (usually either zero-range Skyrme or finite-range Gogny forces) and wave

functions. The equation is then solved iteratively in order to achieve self consistency between the wave functions and the mean field.

$$\left(-\frac{\hbar^2}{2M}\nabla^2 + U\right)\phi_i = \epsilon_i\phi_i$$

Pairing effects are state dependent, and are added by either the BCS or Bogolyubov methods. The HFBCS and HFB mass models of the Brussels group [40] produce an rms error of just over 700keV, but produce worse results for doubly closed shell nuclei, and nuclei further from stability.

An additional mass model known as the P-Scheme model is based on the relationship between the microscopic portion of the nuclear mass with the average number of proton-neutron interactions per valence nucleon[41]. The microscopic mass is obtained by taking the difference between measured nuclear masses and the macroscopic portion of a FRDM calculation. This quantity is defined as the Semi-Empirical Mass (SEM)

$$SEM = M_{tot} - M_{macro}.$$

The average number of proton-neutron interactions per valence nucleon is defined as:

$$P = N_p N_n / (N_p + N_n),$$

where N_p is the number of valence protons or proton holes, and N_n is the number of valence neutrons or neutron holes. Particles are counted when the shell is less than half full, and holes are counted when the shell is more than half full. The SEM is plotted against the P values for a series of nuclei in an isotopic chain, and the resulting curve is fit with a polynomial. With the polynomial calculated from known nuclei, the SEM value can be obtained for nuclei of unknown mass.

SEM vs P for Z=28-50 & N=50-82
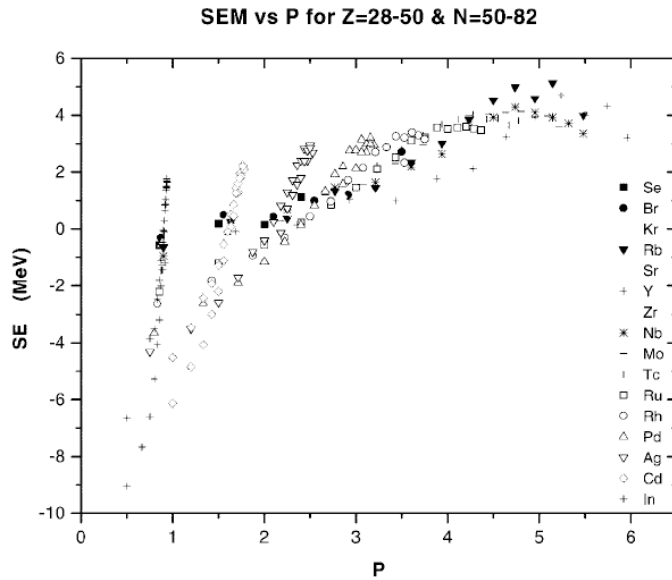
Figure 2.7. SEM vs P value for nuclei between Z = 28-50 and N = 50-82. The behavior of each element can be seen clearly. By fitting each isotopic chain, predictions can be made for the masses of unmeasured nuclei [41].

This representation breaks down at or near the closed shells, where the number of valence particles and holes goes to zero. In these cases, one can use a related parameterization called F-Spin, which is defined as:

$$F_0 = \frac{1}{2}(N_\pi N_\nu),$$

where N_π and N_ν are the number of proton and neutron valence pairs. This overcomes the problems of using the P parameterization at closed shells, but is restricted to even-even nuclei, as only pairs of nucleons are considered. Again the SEM value is plotted, this time against the F_0 value for each nucleus, and a polynomial relationship allows one to calculate mass values for unknown nuclei.

37

2.3 Beta Decay Halflives

Beta decay is a weak nuclear process that converts a neutron in to a proton (or vice versa), while keeping the nuclear mass number A constant. A beta decay also emits a beta particle (electron or positron) and a neutrino. There are several types of beta decay: β^+, β^-, and electron capture. β^+ and electron capture occur in proton-rich nuclei, while β^- occurs in neutron-rich nuclei. The general formula for beta-decay is:

$$\beta^+ : {}^A_Z X_N \rightarrow {}^A_{Z-1} Y_{N+1} + \beta^+ + \nu + Q_\beta$$

$$\beta^- : {}^A_Z X_N \rightarrow {}^A_{Z+1} Y_{N-1} - \beta^- + \overline{\nu} + Q_\beta$$

$$\text{Electron Capture} : {}^A_Z X_N + e^- \rightarrow {}^A_{Z-1} Y_{N+1} + \nu + Q_\beta$$

Q is the amount of energy released in the decay and corresponds to the difference in mass between the parent and daughter nuclei. If Q is greater than zero, the decay has the possibility of occurring.

The beta-decay rate is a function of the transition strengths from the ground state of the parent nucleus to the ground state and excited states in the daughter nucleus with the decay rate described by:

$$\lambda = \frac{m_e^5 c^4}{2\pi^3 \hbar^7} f(Z, E_0) |\Sigma_{\mu M_f} \langle J_f M_f \xi | \mathbf{O}_{\lambda\mu}(\beta) | J_i M_i \zeta \rangle|^2$$

where

$$\Sigma_{\mu M_f} \langle J_f M_f \xi | \mathbf{O}_{\lambda\mu}(\beta) | J_i M_i \zeta \rangle|^2$$

is the reduced transition probability to the final state, and

$$f(Z, E_0)$$

38

is the Fermi function, which describes the effect on the beta particle's wave function due to the Coulomb field of the daughter nucleus.

The decay half-life can be related to the decay constant λ through:

$$\frac{d[N]}{dt} = -N\lambda$$

$$\frac{N}{N_0} = e^{\lambda \cdot t}$$

$$t_{1/2} = \frac{\ln 2}{\lambda}$$

where N_0 is the number of nuclei originally present in a sample, and N is the number of nuclei still present at time t. The emitted electron and neutrino both have intrinsic spin $= 1/2$. There are two possible alignments of the spins then, 1, and 0. These different types of beta-decays are known as Fermi (spins anti-aligned) and Gamow-Teller (spins aligned). If the beta particle and neutrino are emitted with orbital angular momentum $\ell = 0$ (the allowed approximation), the total change in nuclear spin $\Delta J = 0$ for Fermi-type decays, and $\Delta J = 0, 1$ for Gamow-Teller-type decays. The parity change for both types of decays is $\Delta \pi = (-1)^\ell$ so that for allowed decays, the parity will be the same in the initial and final states. The change in isospin $\Delta T = 0$ for Fermi-type decays and $\Delta T = 0, 1$ for Gamow-Teller-type decays. Therefore, the Fermi-type decays proceed mainly through isobaric analogue states (IAS) in the daughter nucleus. Because of the large neutron to proton ratio in r-process nuclei, the parent and daughter generally do not have analogue states near one another, which means that Fermi type decay is unlikely to occur.

In addition to the allowed ($\ell = 0$) decays, there can also be $\ell \neq 0$ or forbidden decays. Decays with $\ell = 1$ are known as first forbidden decays and have $\Delta J = 0, 1$

for Fermi-type decays, and $\Delta J = 0, 1, 2$ for Gamow-Teller-type decays. The parity change for both types is $\Delta \pi = (-1)^{\ell} = 1$. Because of the higher angular momentum, first forbidden decays are less probable to occur than allowed decays by a factor of 1000.

As with nuclear masses, the beta-decay rates for most nuclei involved in the r-process have not been measured. This requires the use of beta-decay rate predictions for use in r-process simulations. Also like with nuclear masses, beta-decay rates have been calculated with either global or microscopic formulas. The global Gross Theory picture treats the beta strength distribution in a statistical manner[?]. It integrates the strength function over the low-lying excited states in the daughter nucleus to get the half-life. Microscopic approaches based on the Random Phase Approximation (RPA) [?] treat low lying excited states in the daughter nucleus as particle-hole excitations of the ground state. These states can be treated as spherical or deformed, with the values of the half-life being strongly dependent on the deformation. Generally, the deformation is determined by a calculation from a mass model. In our case, we have compared our measured values with a RPA calculation using the FRDM mass model. Table 4.1 shows the wide range of half-lives for the region of interest depending on the choice of ground state shape.

CHAPTER 3

EXPERIMENT

3.1   Goals

By performing this experiment we hope to provide information about how the nuclear orbitals and magic numbers change far from the line of stability, and how these changes in nuclear structure affect the r-process abundances. The neutron rich isotopes in the region of Ge-Br approaching $N = 60$ sit in the middle of both of these questions. It has been shown for lighter nuclei that the magic numbers disappear and new magic number appear if enough neutrons are added[24].

As the structure of nuclei change, other nuclear properties also change. This means that beta-decay half-lives, beta-delayed neutron emission ratios, neutron capture rates, and masses can all be very different from their values in more stable nuclei. Changes in these values will affect the abundances produced by the r-process. There have been suggestions that the energy gaps of the neutron closed shells at $N = 50, 82$ are smaller than previously thought[25] [27].

R-Process calculations done with mass models similar except for their shell strength have shown that a significant abundance difference develops. The ETFSI and ETFSI-Q mass models are similar calculations except that the ETFSI-Q model used quenched shell strength, which has the effect of filling in the abundance troughs around the $A = 80, 130,$ and 190 peaks. Because the shells are not as strong the beta-decay half-lives are shorter and material will flow through the region more

smoothly, eliminating the abundance troughs. For alpha-rich freezeout scenarios, neutron rich nuclei in the Ge-Br region may even be the seeds for the r-process.
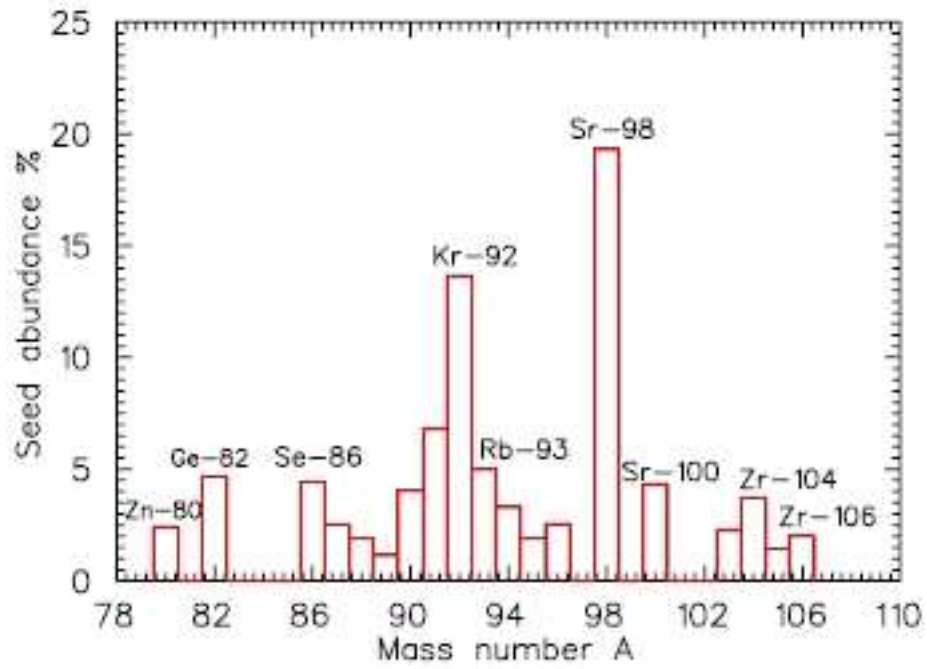
Figure 3.1. Calculated abundance of neutron-rich seeds produced in an alpha-rich freezeout following a core collapse supernova. From [26].

In addition to the nuclear structure questions surrounding the $A = 100$ region, the presence of different "weak" and "main" r-process abundances for $Z < 50$ requires additional nuclear data. Information about the neutron rich Ge-Br isotopes will help to disentangle the contributions from these two different processes, in addition to any other processes that may contribute to heavy element production across the universe.

3.2 Experimental Efforts

The production and study of nuclei far from stability requires specialized facilities. Generally, two methods of production are used: the In-Flight and Ion Separation On-Line (ISOL) techniques. The In-Flight technique uses an energetic beam of stable nuclei that impinges on and reacts with a target. Exotic nuclei are produced through reactions such as Fusion-Evaporation, in which a heavier product nucleus is created; or Projectile Fragmentation, where a lighter product is created. In either case magnetic separation is required to remove unreacted primary beam and uninteresting products from the nuclei of interest. This method can produce a wide range of proton- and neutron-rich nuclei. It is advantageous because the nuclei are produced with velocities near the primary beam velocity, meaning that the production, separation and detection can be done very quickly. In addition there is no dependence on the chemistry of the products as in the ISOL method. There are number of very different facilities that produce nuclei via the In-Flight technique including: the National Superconducting Cyclotron Facility (NSCL) at Michigan State University, TWINSOL at the University of Notre Dame, ATLAS at Argonne National Laboratory, RIKEN in Japan, and the FAIR at GSI in Germany.

Ion Separation On-Line uses a high energy proton beam and a thick target. Exotic nuclei are produced via spallation in the target and must be extracted from it. While this technique can not be used for the shortest-lived isotopes, it can provide high intensities of certain elements, and has the added feature that the isotopes produced may be easily reaccelerated for use in further reactions. ISOL facilities include: ISOLDE at CERN, SPIRAL at GANIL in France, HRIBF at Oak Ridge National Laboratory, and IGISOL in Jyvaskala, Finland.

3.3 Setup

This experiment was performed at the National Superconducting Cyclotron Facility (NSCL) at Michigan State University. The NSCL uses two coupled cyclotrons to accelerate a primary beam onto a target, producing a secondary beam of neutron-rich nuclei. Particle accelerators generally work by accelerating a charged particle through an electric field. To produce a high energy beam either the field must be very strong, or the particle must be passed through it many times. Cyclotrons work by using a magnetic field to bend particles into a circular orbit so that they can be accelerated through an electric field many times.

The particle is injected into the center of the cyclotron and is accelerated in a spiral shaped path. The electrodes in the center are known as "dees" because they have the shape of the letter D. The dees are connected to an alternating current which has a period equal to the orbital period of the particle. This is done so that the particle will be accelerated through both gaps between the dees on each orbit. The time for one orbit is the circumference divided by the velocity of the particle.

$$t = 2\pi r/v = 2\pi mv/Bqv = 2\pi m/Bq$$

Where B is the strength of the magnetic field, m is the mass of the particle, and q is its charge. The orbital frequency is:

$$\omega = qB/m.$$

This value is known as the cyclotron resonant frequency.

The magnets above and below the dees are held at a constant field, so that as the particle is accelerated its orbital radius increases. The force due to the magnetic field is:

$$F = qvxB = mv^2/r$$

so that the force is perpendicular to the direction of the velocity and produces a circular orbit. Therefore the orbital radius is:

$$r = mv/Bq.$$

When the (nonrelativistic) particle reaches the edge of the dees it is extracted with a kinetic energy of:

$$T_{max} = 1/2mv_{max}^2 = (Bq\rho)^2/2m = (B\rho)^2/2(q^2/m)$$

where ρ is the maximum physical radius of the dees. The term $(B\rho)^2/2$ is a parameter that categorizes the capabilities of each particular cyclotron and is known as the K value for the cyclotron. This is where the names of the two cyclotrons at NSCL, the K500 and the K1200, get their names. The K value is often given in units of MeV so that it corresponds to the maximum kinetic energy to which a cyclotron can accelerate a proton ($q = 1$, $m = 1$).

At NSCL the cyclotrons have magnets broken up into high- and low-field sectors. This is done in order to provide vertical focusing for the beam. Additionally, trim coils are added to increase the magnetic field, in order to deal with the increase in mass of the beam particles due to relativistic velocities. The ratio B/m appears in the equation governing the cyclotron resonant frequency, so for an increase in mass of:

$$m = \frac{m_0}{\sqrt{(1 - (v/c)^2)}}$$

the magnetic field must be increased by the trim coils in order to maintain the cyclotron frequency.
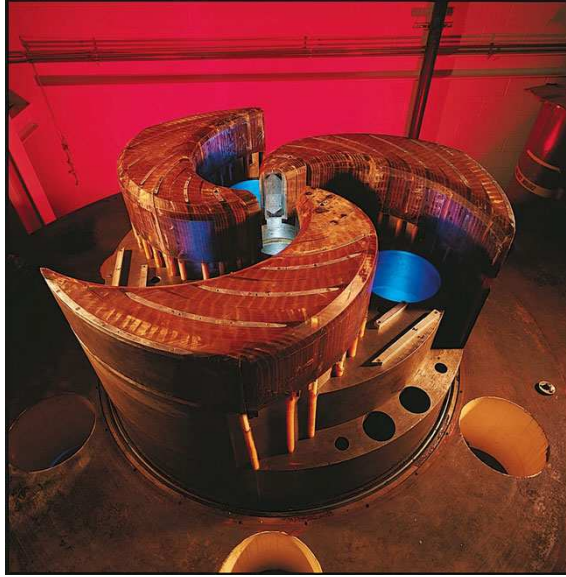
Figure 3.2. K1200 Dees and trim coils during installation. From NSCL image library.

The first cyclotron, the K500, accelerates the primary beam of ^{136}Xe to an energy of 10.85MeV/U. The beam is then passed through a stripper foil and injected into the second cyclotron, the K1200. Next, the second K1200 cyclotron accelerates the beam to an energy of 120MeV/U. The average intensity of the primary beam was $2pnA$.

The primary beam strikes a $240mg/cm^2$ Be target and fragments into many lighter neutron-rich nuclei. The fragments are produced with a kinetic energy that is a large fraction of the primary beam, and proceed in forward direction to the A1900 fragment separator [48]. Along with the fragments there is also degraded primary beam that must be removed by the separator. This method of producing a radioactive beam is known as Projectile Fragmentation. It provides fast production

and transport of radioactive nuclei, so that isotopes with very short half-lives may be studied. Additionally, unlike the slower ion separation on line (ISOL) technique, Projectile Fragmentation does not depend on the chemistry of the primary beam or secondary products. While not utilized in this experiment, the radioactive beam could be used on a secondary target to produce even more exotic tertiary products.
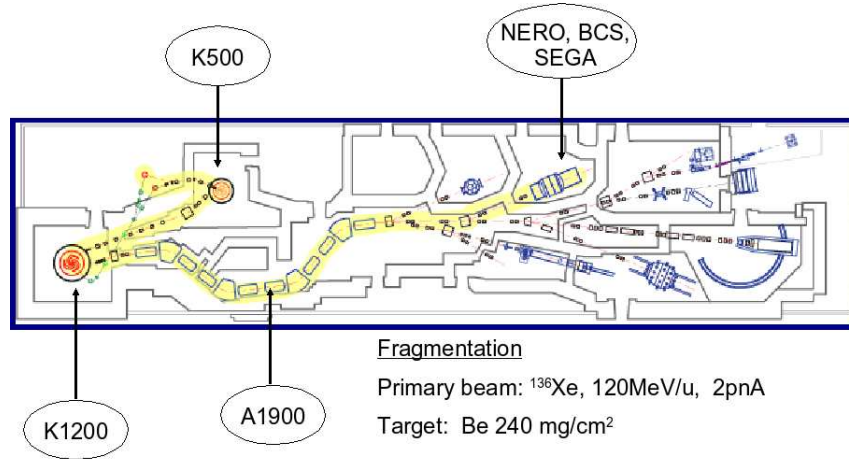
Figure 3.3. Layout of the NSCL showing the K500 and K1200 cyclotrons, A1900 fragment separator and location of the experimental vault used for this work. From NSCL image library.

In order to separate nuclei of interest from unwanted fragment nuclei and unreacted primary beam, a magnetic separator system called the A1900 is used at the NSCL. It is composed of four superconducting dipole magnets to bend the beam, and forty quadrapole and higher multipole magnets used to focus the beam. A dipole magnet with radius (r) and field strength (B) , bends an ion with a given mass (m) and velocity (v) according to the following equation:

$$\gamma m v = q B r$$

Two dipoles will produce a focused beam with a momentum to charge ratio

determined by the magnetic rigidity value obtained for a particular choice of the magnetic field B. The location where this focus occurs is called the intermediate focal plane. Nuclei with a different momentum to charge ratio are blocked by slits at the focal plane and will not pass through. Nuclei produced in the fragmentation reaction have similar velocities, so selection by the dipoles is essentially a selection of nuclei with particular mass to charge ratios. To separate nuclei with similar m/q ratios but different Z than the nucleus of interest, a degrader is also placed at the focal plane. The energy loss for each nucleus in the degrader is given by the Bethe formula:

$$-\frac{dE}{dx} = \frac{4\pi e^4 z^2}{m_0 v^2 A} N_A \rho B(v)$$

with

$$B(v) = Z \left[\ln \frac{2m_0 v^2}{I} - \ln \left(1 - \frac{v^2}{c^2} \right) - \frac{v^2}{x^2} \right]$$

where z is the charge of the nucleus, v is its velocity, ρ is the density of the degrader material and N_A is Avogadro's number.

Therefore each isotope will have a different momentum after passing through the degrader. A second set of dipoles will again select a particular momentum, filter out unwanted nuclei and transmit those that are of interest. For this experiment the magnetic rigidity of the dipole magnets was tuned to pass ^{88}Se. A position sensitive plastic scintillator was placed at the dispersive focal plane to act as a degrader, and to provide a measure of the horizontal position of each isotope. The scintillator was also used as the start for time-of-flight measurements. In addition an aluminum "finger" was placed at the dispersive focal plane in order to block ^{136}Xe charge states that were present there. Nuclei that were passed through the A1900 were then sent to the N3 experimental vault.

3.4 Particle ID

To identify individual nuclear species, two methods were used. The first was to do an identification of one nucleus by measuring a decay from an isomeric level. Isomers are states in a nucleus that exist for a long time before decaying via gamma decay. The decay emits a gamma ray of a unique energy that can be used as a unique signature from one particular nucleus. Once one nucleus was unambiguously identified, the rest could be identified through a $\Delta E - ToF$ plot. This sort of plot separates nuclei according to A and Z. The energy loss of a nucleus passing through a detector is also given by the Bethe formula, so that for a nucleus fully stripped of electrons:

$$dE \propto Z^3/A$$

The time-of-flight is:

$$ToF = d/v = dA/p$$

where d is the distance from the the A1900 focal plane to the N3 experimental vault and p is the momentum of the nucleus. Thus a $\Delta E - ToF$ plot will separate nuclei by Z and A, which enables gating on a single nucleus in order to study its beta decay properties.

Isomeric decays are used for the ID because the distance from the target to the N3 vault is approximately 40 meters. The time of flight for the secondary beam will then be around 500ns. This time delay ensures that prompt gamma decays have already occurred, but that isomeric states will still be populated. An isomeric level of over 1μs was desired to ensure a sufficient counting rate. For this experiment a 8.6μs isomeric state in ^{99}Y was used. With this isotope identified, the remaining

49

nuclei could be identified as well.

In order to measure the 126keV gamma ray from the isomeric state of ^{99}Y, three HPGe detectors were used. These detectors come from the Segmented Germanium Array (SEGA) at MSU. Germanium detectors are semiconductor detectors that work by transmitting the energy of an incoming photon to the valence band electrons mainly by Compton scattering. The increased energy of the electrons promotes them to the conduction band, where they can be collected by an anode at a high potential. Germanium detectors are preferable because they have a high detection efficiency and an energy resolution of 3-4keV.

A different implant station was used for this part of the experiment. It consisted of a thick aluminum plate placed perpendicular to the beam in the N3 vault, with a Silicon PIN ΔE detector placed in front of the plate. A PIN detector is a silicon diode made up of three layers: a p-type (hole doped) layer, an intrinsic (no doping) layer, and an n-type (electron doped) layer. The intrinsic layer acts as a large depletion region in which electrons and holes are created by the incoming radiation. A reverse bias is applied to the detector, which causes the electrons to move toward the p-type material where they are collected by a terminal. These electrons compose the signal to be amplified and used as the ΔE value.

The three Ge detectors were placed around the beam pipe at the location of the plate. Nuclei passed through the two plastic scintillators giving a ToF signal, and through the PIN detector giving a ΔE signal. They were then implanted into the aluminum plate, without being implanted into the Beta Counting System (BCS). Once implanted, the isomeric states decayed and were detected by the Ge detectors. The $\Delta E - ToF$ spectrum could be gated on events that produced the 126keV gamma rays. This gated spectrum then showed which events were from ^{99}Y.
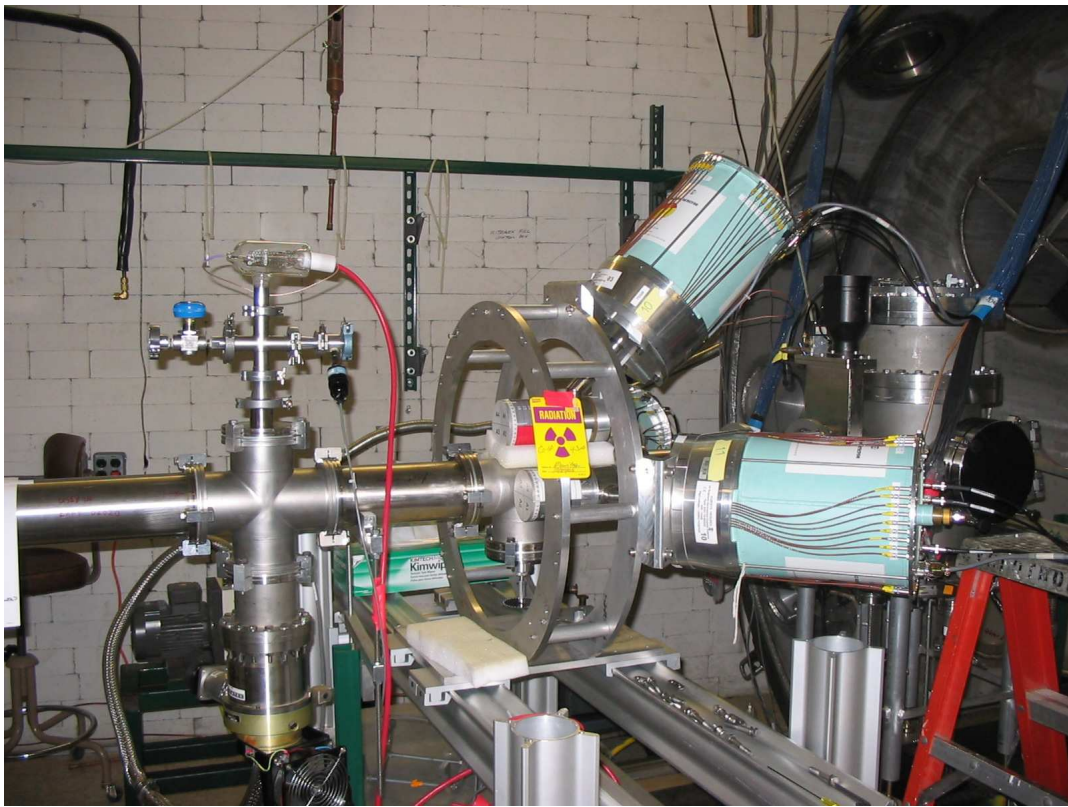
Figure 3.4. SEGA germanium detectors surrounding the implantation plate.

3.5 Detector setup

In the N3 vault, nuclei were implanted into the BCS. The BCS consists of four silicon PIN detectors, one double sided silicon strip detector (DSSD) and one single sided silicon strip detector (SSSD)[49]. The DSSD and SSSD detectors are similar to the PIN detectors except that they include multiple terminals that are separated from one another. Therefore these detectors are able to be read out in individual strips. Our setup also included a 1000μm thick Ge detector behind the silicon detectors. The Ge detector was tested for use in identifying gamma rays from implanted nuclei, but this proved to be ineffective. Instead, the Ge detector was used to veto light particles (Chapter 4).
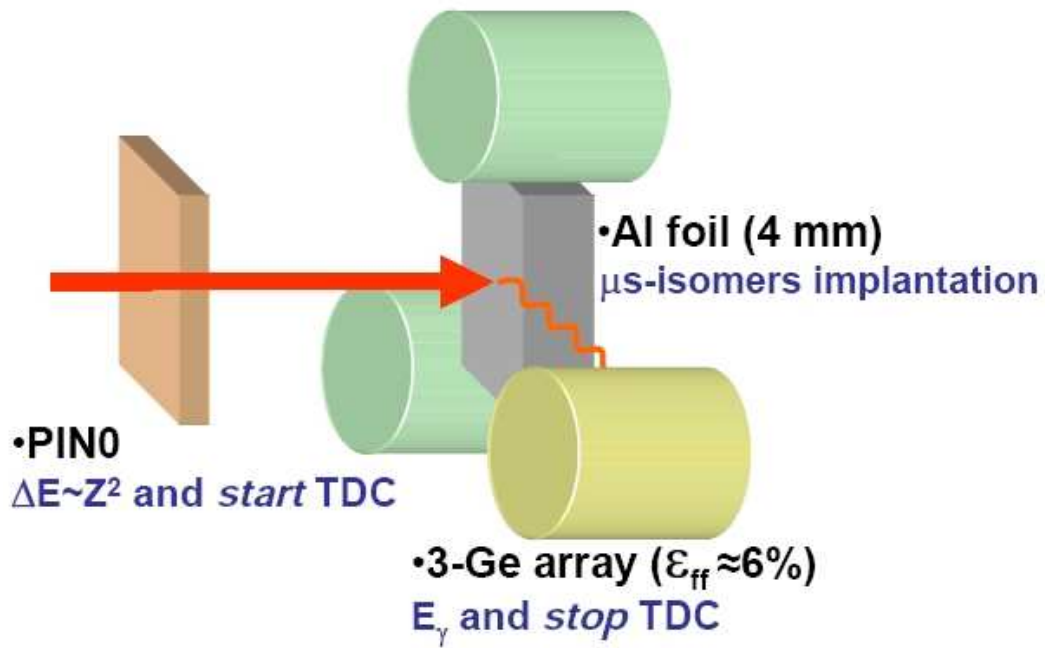
Figure 3.5. Schematic drawing of the setup of the SEGA detectors and aluminum implant plate used for particle id. Pin 0 was used as the dE detector in this setup, while the same scintillators (not shown) used in the rest of the experiment provided the particle time-of-flight.

The four PIN detectors had thicknesses of 991μm, 303μm, 309μm, and 966μm. The DSSD had a thickness of 979μm, and the SSSD had a thickness of 988μm. These thicknesses were chosen so that nuclei were implanted into the DSSD, which was segmented into forty 1mm strips on the front and forty perpendicular 1mm strips on the back, giving 1600 pixels. The output from the DSSD was sent to a dual-gain preamplifier (2V/pC and 0.1V/pC), enabling it to detect both implanted nuclei and beta decays. Each implant or decay event was recorded with the pixel location and time stamp in addition to the energy of the event. The SSSD was made up of sixteen strips and was used to veto light particle implantations not stopped in the DSSD, as well as detect beta decay events that did not deposit all of their

energy in the DSSD. Typically implantation rates were 1×10^{-3}implants/s/pixel.
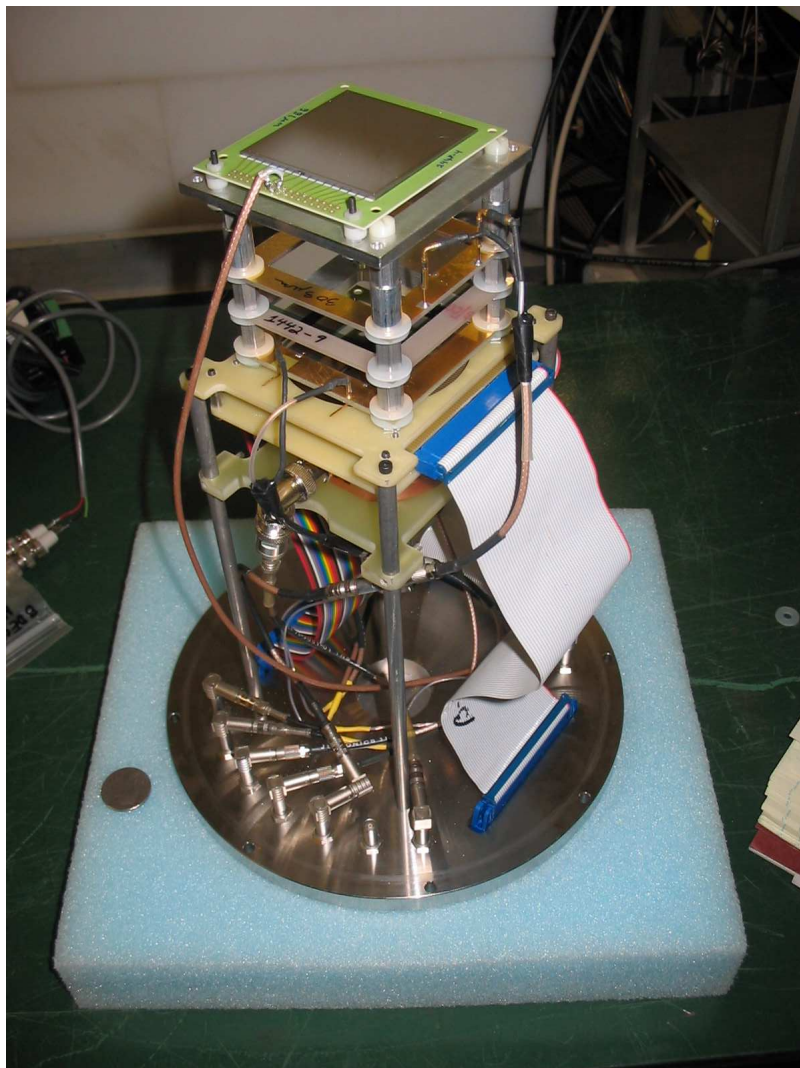
Figure 3.6. BCS detectors. The four PIN detectors can be seen in addition to the ribbon cable connected to the DSSD.

In order to detect the beta delayed neutron, the Neutron Emission Ratio Observer (NERO) detector system was placed around the BCS setup. NERO is made up of 60 proportional neutron counters placed in a polyethylene moderator. There is one ring of 16 ^{3}He detectors, surrounded by two concentric rings with 20(inner) and 24(outer) BF_3 detectors. The design was chosen to maximize the detection ef-

ficiency of the detector. Neutrons are detected via the $^3\text{He}(n,d)^3\text{H}$ and $^{10}\text{B}(n,a)^7\text{Li}$ reactions. The cross section for these reactions is highest in the thermal neutron regions En ~ 0.0025eV. The neutrons must therefore be moderated, which is done by the polyethylene block they are seated in. The anode of the detectors measures the energy from the deuteron and alpha particles respectively. The energy of the neutron is much smaller than the Q value for these reactions, which are $0.764\text{MeV}(^3\text{He})$ and $2.792\text{MeV}(BF_3)$, so the energy detected is essentially these Q values. Thus the energy information the neutrons is lost, but we are concerned with the number of neutrons detected, not their energy. When a beta decay was detected in the DSSD, NERO was gated to look for neutrons for 200μs. This amount of time was chosen to allow sufficient time for the neutrons to be moderated by the polyethylene block.

3.6   Electronics

The experimental logic is shown in Figure 3.11. The master trigger for the experiment was either a signal in PIN1 from an implant nucleus or a beta decay event from the DSSD. An additional master trigger was created from the three germanium detectors timing signals when the SeGA setup was used. The master trigger live was created by using the master trigger and a NOT busy signal from the acquisition computer, and was used to trigger the acquisition computer and to create gates for the acquisition components and logic.

Signals from the PIN detectors were sent to preamplifiers and then to amplifiers with energy(slow) and timing(fast) outputs. The energy outputs were sent to VME ADC modules, while the timing outputs were sent to a VME TDC, a scaler module and a coincidence register.

Energy signals from the SeGA detectors were sent to a spectroscopy amplifier and then to a CAMAC ADC. The timing signals were sent to a scaler module and
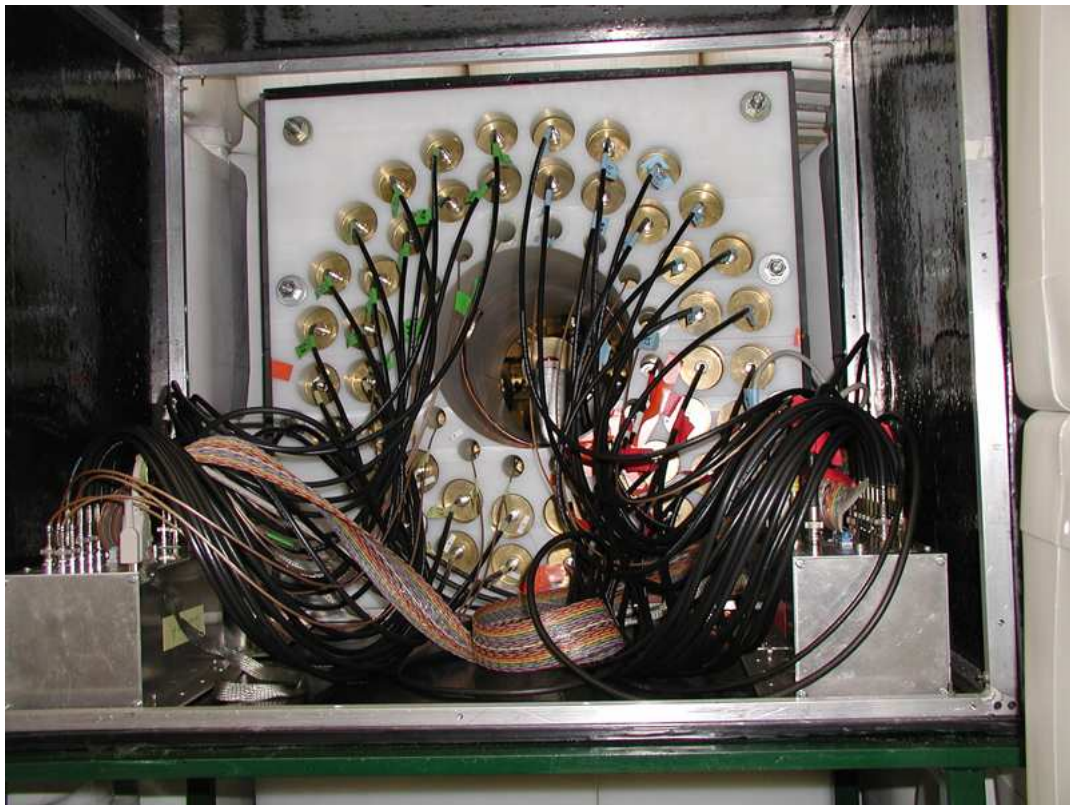
Figure 3.7. NERO detector. The inner ring of ^{3}He detectors and the outer rings of BF_3 detectors can be seen. Though not pictured here, the BCS detectors sit inside central cavity during the experiment.

a TDC. They were also combined in an OR to create the SeGA trigger.

The signals from the forty front DSSD strips and the forty back DSSD strips were sent in three groups (1-16, 17-32, 33-40) to Multichannel Systems preamplifiers. These preamplifiers were able to output signals with two different gains in order to distinguish between implant events and beta decay events. The low gain signals were sent directly to VME ADCs, while the high gain signals were sent first to shaper/discriminator modules and then to VME ADCs and scaler modules. The high gain signals were also combined in a logical OR and sent to a VME bit register. This bit was used to readout DSSD strips that had a signal from one strip in their
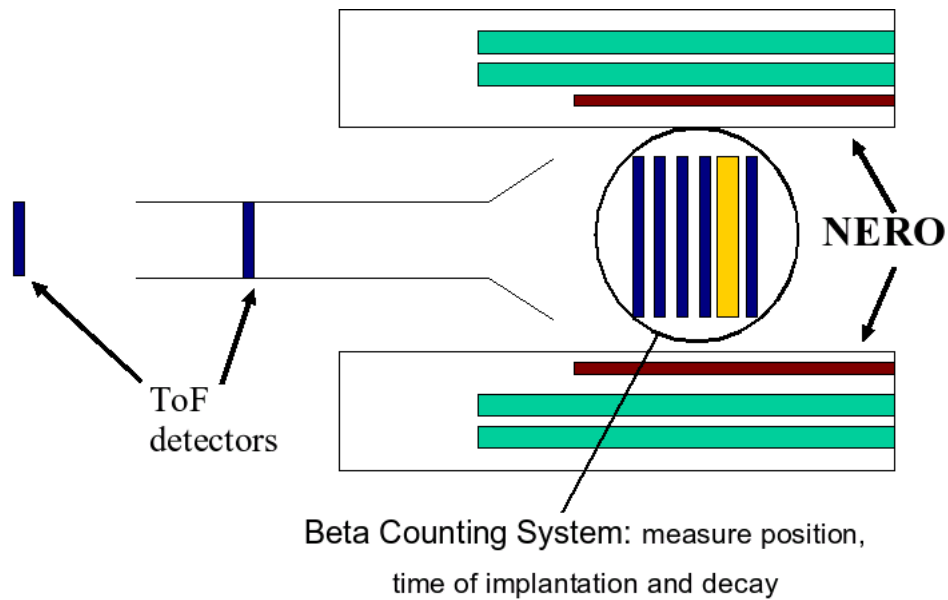
Figure 3.8. Schematic drawing of the time-of-flight, BCS, and NERO detectors used in this experiment.

group (1-16, 17-32, 33-40).

NERO signals were read out in four quadrants of fifteen detectors each. The signals were sent through a preamplifier and then to a shaper/discriminator. The shaper signals were sent to a VME ADC. The fast discriminator signals were sent to VME TDC and scaler modules. The NERO master gate was created by the master gate generated by a beta decay event in the high gain DSSD signals. A master gate live was made by the AND of the master gate, a $200\mu s$ gate generated after a master gate live signal, and a not bust signal from the acquisition computer. This master gate live was used to set a window to readout the NERO ADCs so that neutrons only within $200\mu s$ of a beta decay were recorded.

Legend: (100) Is a 100 ns delay
Numbers: crate,slot.channel

N3 Sci. Anode — Split — Split (To data U S) — ΔMP — VME ADC

S p l i t

CF D — N3Sci Trigger

Stop
Start
VME TDC
Bit ?
Scaler

IM2 N Sci — CF D

IM2 S Sci — CF D

Start / Stop — TAC Gate — Attenuator — VME ADC
Scaler
Start / Stop — TAC — Attenuator — VME ADC
Stop / Start — VME TDC
Stop / Start — TAC — VME ADC
Stop / Start — VME TDC
Scaler

ADC VME,1-6

All ADC's:
  Ch. 1-16: Hi
  Ch.17-32: Lo
Order:
• front 1-16
• front 17-32
• front 33-40
• then same for back

Cycl. RF — CF D — Start / Stop — TAC — VME ADC
VME TDC
AND — Scaler

Pin 1 — PA — Amp — CF D — NIM-ECL — PIN 1 Trigger

VME ADC
Stop / Start — VME TDC
Bit ?
Scaler

• Pin1, Pin1a,
  Pin2, Pin2a:
  Implants
  (PA, AMP)
• Pin3-4:
  Electrons
  (PA, AMP)

Pin 2-4 — 3 PA Quad 3 — Amp — slow / fast — CF D 3x — NIM-ECL — PIN Trigger
3x 3 fast

VME ADC
Stop / Start — VME TDC
Bit ?
Scaler

BCS Ge ?

GG

SSSD1 — 1x16 PA 1x16 — 6x Shaper Disc 6x16 / 6x16 — VME ADC 7 — GG SSSD
Scaler 4,5,6
CFD 6x — Bit CHECK

DSSD — 80 16x PA 80 Lo / 80 Hi — 6x Shaper Disc — VME ADC 1-6 — GG DSSD
VME ADC 1-6
Scaler 4,5,6
5x — VME Bit 9
Scaler 1,23,0

DSSD Front / DSSD Back — AND — DSSD Trigger

MG

Bus — Busy Latch — NOT — AND — Master Gate Live
Reset / Set
Clear

NIM-ECL — VME Bit 9
NERO "Timeout"
SeGA "Timeout"
NIM-ECL — VME Scaler
NIM-ECL — VME Scaler / NERO In NERO crate

Set — Trigger Latch — VME I/O In0

Trigger Acknowledge

Figure 3.9. Schematic of the beta-detection electronics setup.

CHAPTER 4

DATA ANALYSIS

4.1   Particle Identification

Particle ID was done with the dE-ToF technique. Both the energy and time-of-flight signals needed to be momentum corrected because the A1900 spectrometer had a momentum acceptance of about 4%. The energy loss, when velocity corrected for the time of flight, gives elemental (Z) separation. The time of flight, when momentum corrected via the focal plane position, gives isotopic (A) separation.

4.1.1   Energy Loss

The energy deposited in the dE detectors by projectile nuclei is characterized by the Bethe Formula:

$$-\frac{dE}{dx} = \frac{4\pi e^4 z^2}{m_e v^2 A} N_A \rho B(v)$$

With:

$$B(v) = Z \left[\ln \frac{2m_e v^2}{I} - \ln \left(1 - \frac{v^2}{c^2} \right) - \frac{v^2}{x^2} \right]$$

where e is the electron charge, Z is atomic number of the detector material, m_e is the electron mass, v is the velocity of the projectile nucleus, A is the atomic weight of the detector material, N_A is Avogadro's number, rho is the mass density of the

detector material, and I is the average excitation and ionization of the detector material.

Because the energy of the projectile nuclei has a velocity dependence, a correction is required to separate nuclei with different Z.

$$Z = \sqrt{\frac{dE}{dx} \frac{m_e v^2 A}{4} \pi e^4 z^2 N_A \rho B(v)}$$

In the experiment the time-of-flight was measured, not the projectile velocity, so the simple relation v = D/t is used to obtain the velocity. The distance D is the total flight path from the focal plane of the spectrometer to the experimental vault, which is essentially the same for all nuclei. A linear correction to the energy was used of the form:

$$dEcorr = dE - M \times ToF + B$$

where M is the slope and B is the intercept. The raw dE-ToF spectrum is shown in fig 4.1 while the corrected spectrum is shown in figure 4.2.
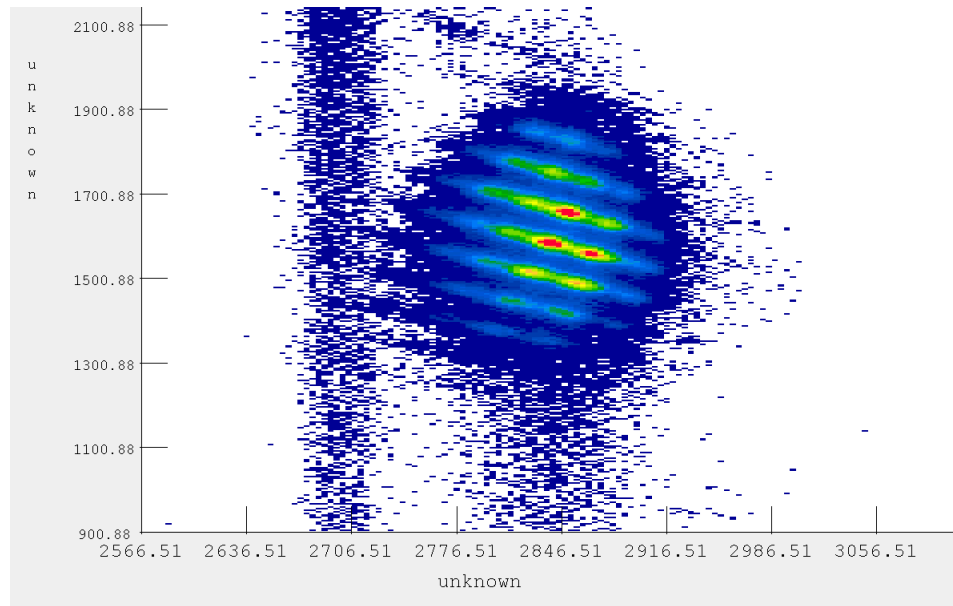
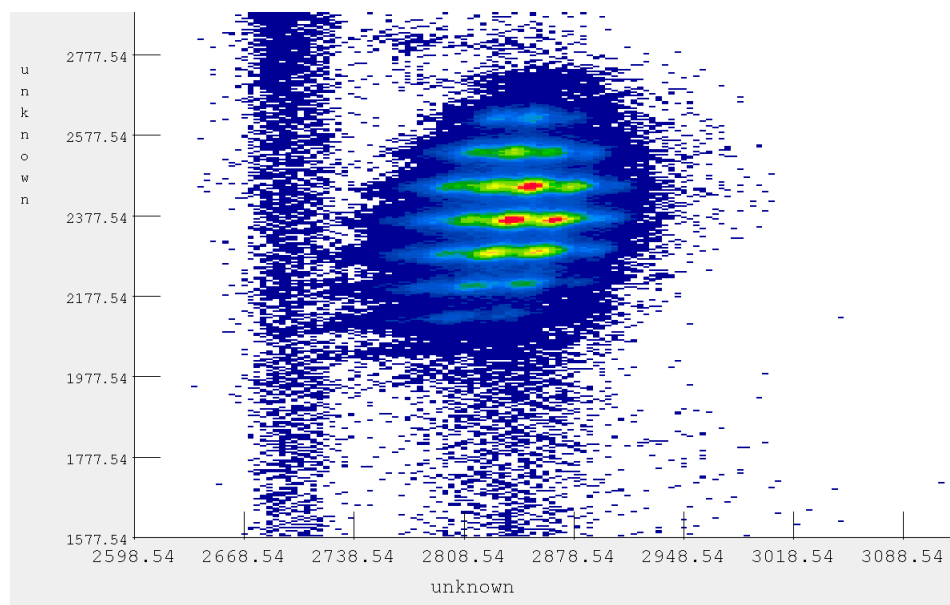Figure 4.1. PIN1 vs ToF, both uncorrected.

Figure 4.2. PIN1 vs ToF. PIN1 corrected, Tof uncorrected.

4.1.2 Time of Flight

The time-of-flight measurement is used to distinguish between different masses of each isotope. From the following equation we can see the mass and momentum dependence on the time-of-flight.

$$ToF = D/v = Dm/p$$

The momentum of nuclei is not directly measured in our experiment, but the magnet settings of the spectrometer define the momentum to be accepted through the equation:

$$B\rho = p/q$$

so that

$$ToF = \frac{mD}{B\rho q}$$

The 4% acceptance of the spectrometer means that there is a distribution in time-of-flight for each mass. Using a correction for the momentum gives a unique ToF for each mass m. We used a linear correction for the momentum dependence of the time-of-flight. This is based on the horizontal position of each nucleus at the image 2 focal plane of the spectrometer.
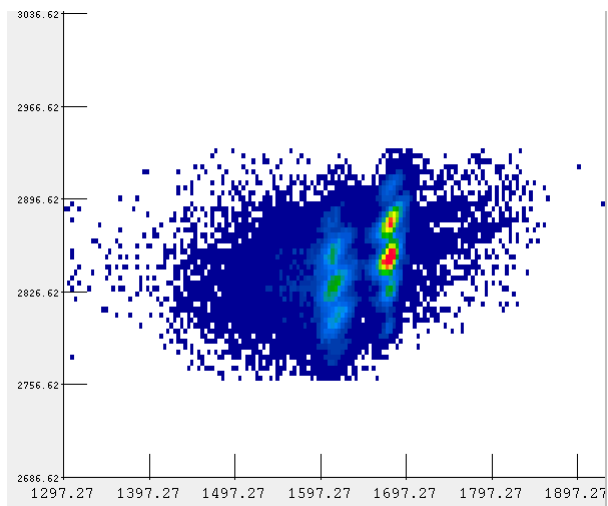
Figure 4.3. ToF vs focal plane position for Yttrium isotopes. Tof uncorrected. Lack of counts between the two sets is due to the presence of aluminum "finger" to block out unreacted primary beam.
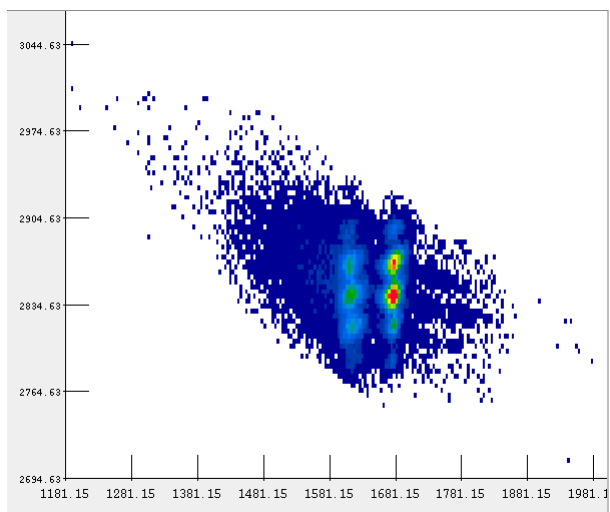

Figure 4.4. ToF vs focal plane position for Yttrium isotopes. Tof corrected for momentum dependence.

4.2 Gain Matching

The high gain outputs of the DSSD and SSSD were gain matched using a ^{241}Am source before the experiment. The source was placed just in front of the DSSD and SSSD.
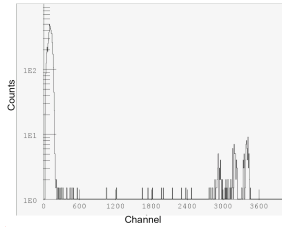
Figure 4.5. Spectrum from ^{241}Am source.

4.3 Thresholds

Low energy thresholds for the high gain outputs of the DSSD and SSSD were set using a ^{90}Sr source. Figure 4.6 shows the spectrum from a typical DSSD strip.
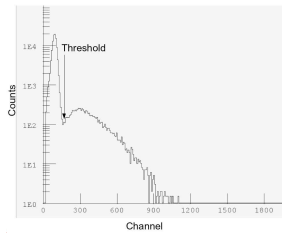
Figure 4.6. Spectrum from ^{90}Sr source.

4.4 Event Definitions

Implant events were defined as events that had a signal in PIN1, and low gain signal in the front and back of the DSSD. Events that produced a low gain signal in

the SSSD were rejected. For events with a signal in more than one strip on the front or back sides, the strip with the maximum energy was recorded as the strip in which the event took place. The pixel location (front and back strip numbers) and the time of implantation were recorded for each event. Decay events were defined as events that did not have a signal in PIN1 or PIN2, and produced a low gain signal in the front and back of the DSSD. Events that produced an overflow signal in the small Ge detector behind the SSSD were rejected. This was done to reject light particles coming with the beam that could be confused with beta decay events from implant events. For decay events, like with implants, when a signal in more than one strip on the front or back sides occurred, the strip with the maximum energy was recorded as the strip in which the event took place. To be considered as decays correlated with implantations, decay events had to come within a ten seconds of an implant. Decay events to one pixel away from the implant were considered valid. Up to three decay events (ie. mother, daughter, granddaughter) within the ten second window were recorded. The decay time for each decay event was the difference between the implantation event time and the decay event time. A window from forty seconds after an implant event in a particular pixel until the next implantation in the same pixel was used to determine background. Any decay event that occurred in this window was considered to be a background event.

4.4.1 Charge State Contanimants

To distinguish between fully stripped nuclei of interest and contamination from hydrogen-like nuclei with mass A+2,3 the total kinetic energy of each nucleus was looked at. In our experiment the pre-amplifiers for the DSSD were saturated for many implant nuclei, thus the DSSD could not be used to determine the total kinetic energy. However,the sum of the energy in the four PIN detectors was sufficient to

distinguish between fully stripped nuclei and charge state contaminants. Gates were drawn in the image 2 focal plane position versus the PIN energy sum plot in order to exclude charge state nuclei.
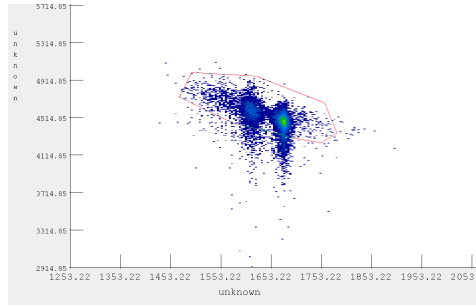
Figure 4.7. PIN1,PIN2,PIN3, and PIN4 energy sum vs focal plane position for ^{99}Y. Charge state contaminants have a lower total kinetic energy, and were therefore excluded by the gate shown.

4.4.2 PIN1 PIN2 Gate

In order to reject light particle and primary-beam contaminants, a gate was made on the PIN1 vs PIN2 spectrum. Figure 4.8 shows this plot, and the gate used.
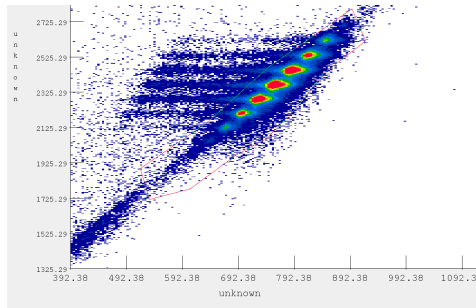

Figure 4.8. PIN1 energy vs PIN2 energy. Counts outside the gate were excluded.

4.4.3 Time-of-Flight Gate

Two photo tubes, one on each side of the image 2 scintillator were used to measure the time-of-flight. Because of a high primary beam rate at the image 2 focal plane, the image 2 scintillator began to fail during the experiment. This was manifest through failing to produce a signal for some particles. This resulted in some events with spurious ToF signals. These events were rejected by creating a gate in the N-ToF vs S-ToF spectrum. This spectrum is the time-of-flight from one photo tube (N-ToF) versus the time-of-flight from the other photo tube (S-ToF). Figure 4.9 shows this plot with the gate used.
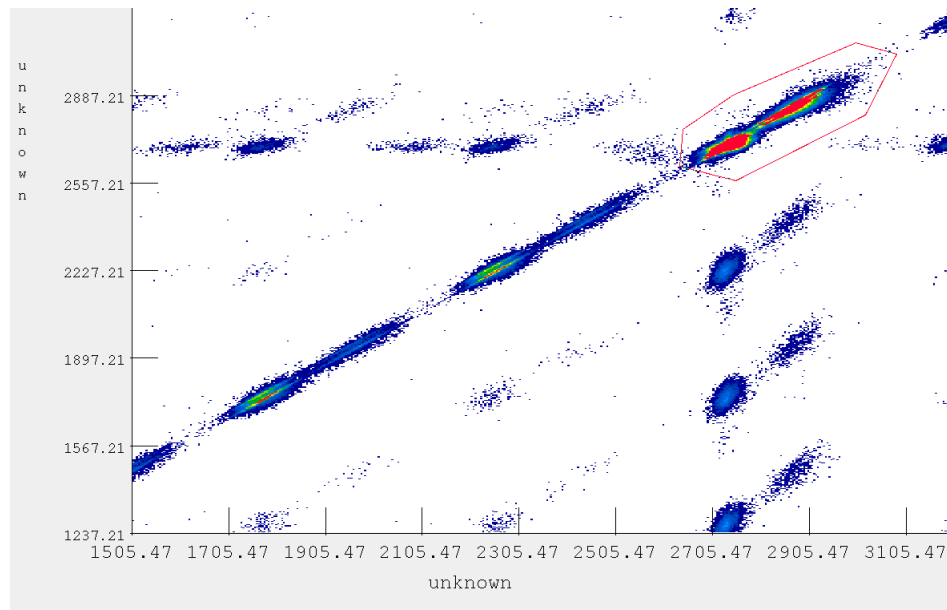

Figure 4.9. N-ToF vs S-Tof. Counts outside of the gate shown were excluded.

4.5 Determining Halflives

4.5.1 Fitting Curves

For the isotopes with high statistics, the beta-decay half life could be obtained through a fit of the decay curve. The decay times for each isotope were put into

bins of 100-400 ms to form decay curves. The curves were then fit using exponential parent, daughter, granddaughter, and constant background components. These equations give the activity at a time t, and are known as Bateman equations.

$$A_n = N_0 \sum_{i=1}^{n} c_i e^{-\lambda_i t}$$

where

$$c_m = \frac{\prod_{i=1}^{n} \lambda_i}{\prod_{i=1}^{n} \prime(\lambda_i - \lambda_m)}$$

The expression for the total number of decays seen at time t becomes:

$$N = C_1 e^{-\lambda_p t} + D_1 e^{-\lambda_p t} + D_2 e^{-\lambda_d t} + G_1 e^{-\lambda_p t} + G_2 e^{-\lambda_d t} + G_3 e^{-\lambda_g t} + B$$

with

$$C_1 = N_0$$

$$D_1 = \frac{\lambda_d N_0}{\lambda_d - \lambda_p}$$

$$D_2 = \frac{\lambda_d N_0}{\lambda_p - \lambda_d}$$

$$G_1 = \frac{\lambda_d \lambda_g N_0}{(\lambda_d - \lambda_p)(\lambda_g - \lambda_p)}$$

$$G_2 = \frac{\lambda_d \lambda_g N_0}{(\lambda_p - \lambda_d)(\lambda_g - \lambda_d)}$$

$$G_3 = \frac{\lambda_d \lambda_g N_0}{(\lambda_p - \lambda_g)(\lambda_d - \lambda_g)}$$

where λ_p is the decay constant of the parent nucleus, λ_d is the decay constant of the daughter nucleus, and λ_g is the decay constant of the granddaughter. B is the value of the background, which is assumed to be constant. The halflife was determined by minimizing the chi-squared of the fit, with the parent halflife, initial parent scaling, and background being free parameters. The daughter and granddaughter halflives were treated as fixed parameters.

Figure 4.10. Decay curve for ^{91}Br with mother, daughter, granddaughter and background components.

Figure 4.11. Decay curve for ^{93}Kr with mother, daughter, granddaughter and background components.

68

Figure 4.12. Decay curve for ^{94}Kr with mother, daughter, granddaughter and background components.

Figure 4.13. Decay curve for ^{95}Rb with mother, daughter, granddaughter and background components.

69

Figure 4.14. Decay curve for ^{96}Rb with mother, daughter, granddaughter and background components.

Figure 4.15. Decay curve for ^{96}Sr with mother, daughter, granddaughter and background components.
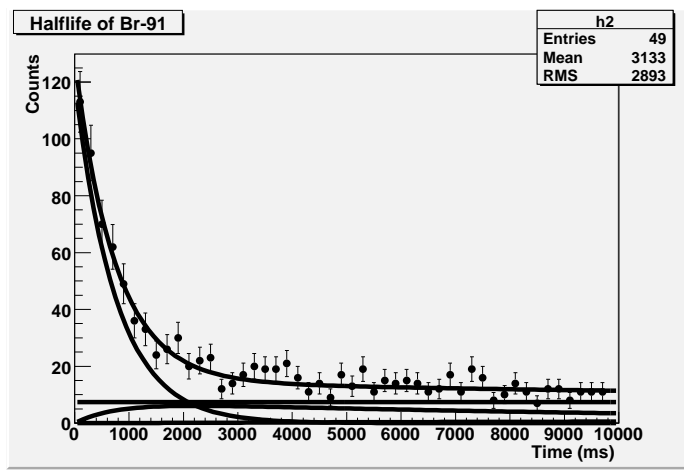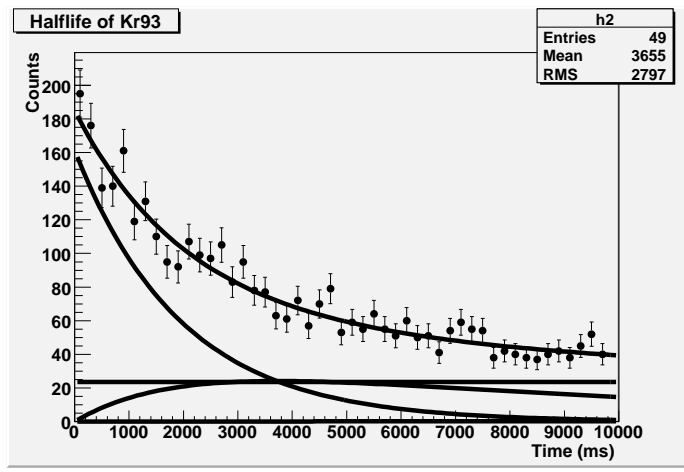
Figure 4.16. Decay curve for ^{97}Sr with mother, daughter, granddaughter and background components.

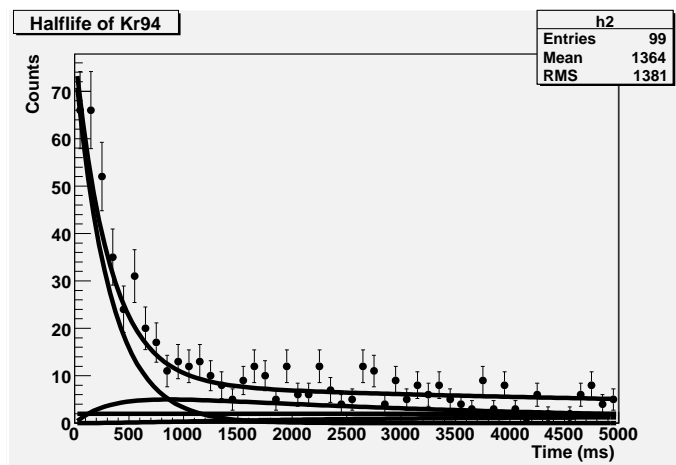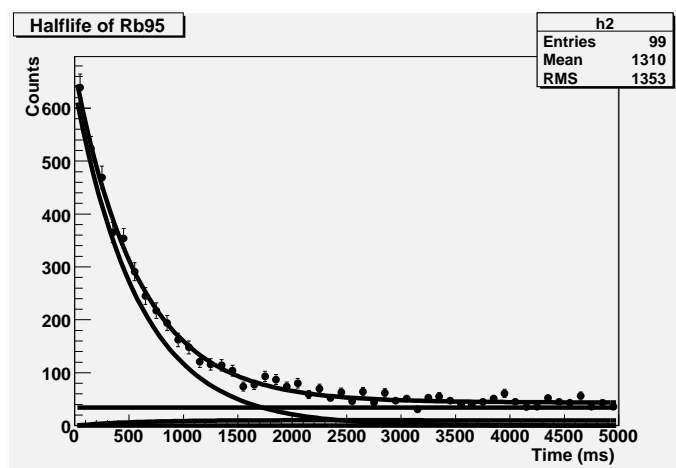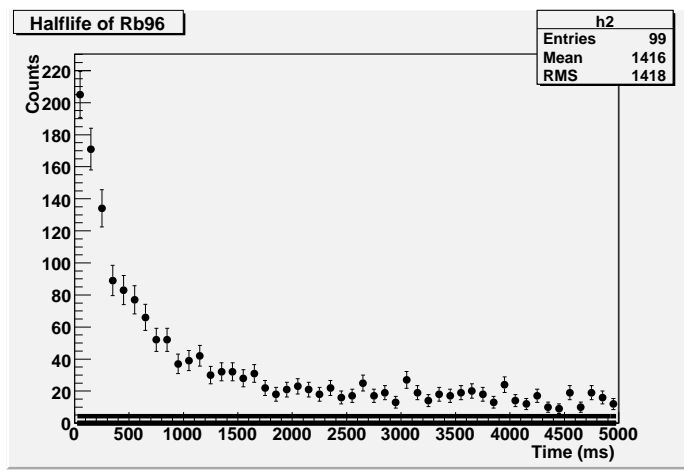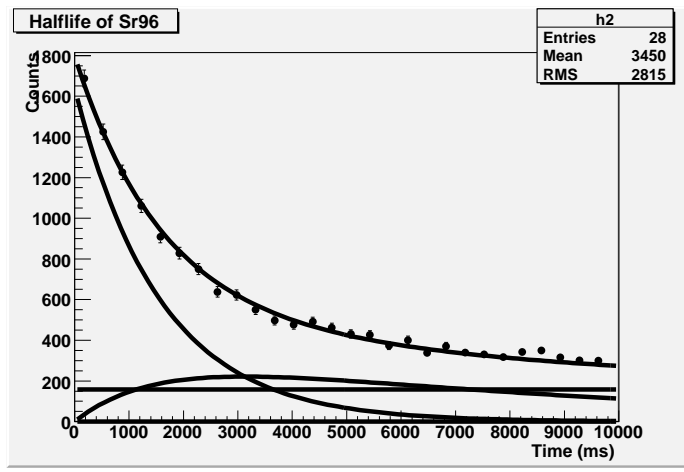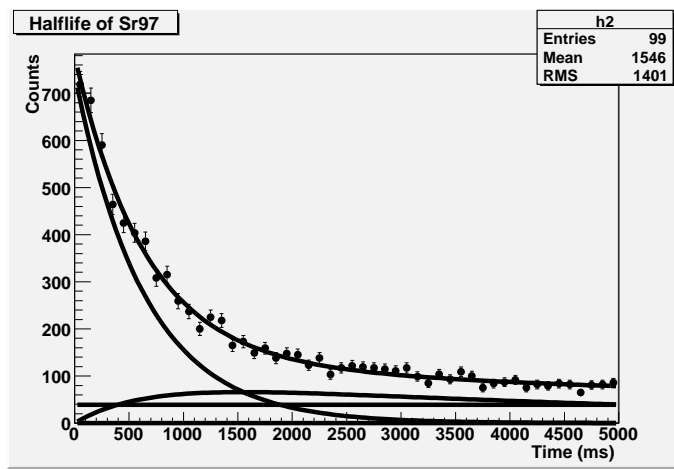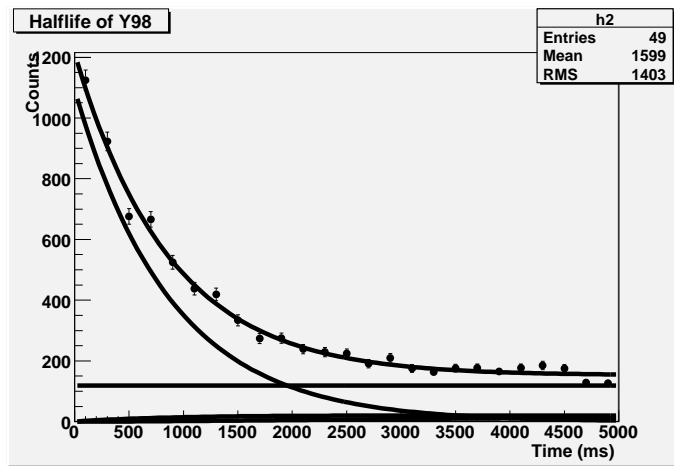Figure 4.17. Decay curve for ^{98}Y with mother, daughter, granddaughter and background components.

71

4.5.2 Beta Detection Efficiency from Decay Curve Fits

The DSSD beta detection efficiency could be determined from the parameters of the decay curve fits. This is an input parameter for the Maximum Likelihood fit. The efficiency is taken as the number of parent beta decays detected divided by the number of parent implants detected. The number of implants can be simply counted from the particle-id spectrum, but because the number of beta decays detected for each isotope is a combination of parent, daughter, and granddaughter decays, the total number of decays for each isotope gate can not be used for calculating the DSSD efficiency. The number of parent decays can be obtained from the parent activity calculated in the above Bateman equation:

$$N_D^{parent} = \frac{(A_o)_{fit}}{\lambda_{fit}}$$

therefore

$$\epsilon_\beta = 100 \times \frac{N_D^{parent}}{N_I}$$

4.5.3 Maximum Likelihood Method

For the isotopes with few events, fitting a decay curve is not possible, so another method of determining the half-lives was needed. We used the Maximum Likelihood Method (MLH), which has been used before for cases of poor statistics[?][?]. This method uses the Bateman equations to determine the probability that beta decays with a given half-life will occur at the times seen in the experiment. The half-life of the parent is varied so as to maximize the probability. That maximizing value is assigned as the half-life of the parent nucleus.

More specifically, the likelihood is joint probability of observing parent, daughter, granddaughter, and background events for a particular value of the beta decay

constant. The beta detection efficiency, beta decay background, daughter and grand-daughter half-lives, beta delayed neutron emission ratios (P_n), and delayed neutron emission daughter and granddaughter half-lives need to be known.

The likelihood function to be maximized is made up of the probability density function for the observance of zero, one, two, or three decays at a given time t. The probability density for a parent decay at a time t, given the decay constant λ_1 is:

$$f_1(\lambda_1, t) = \lambda_i e^{-\lambda_1 t}$$

The probability for a parent decay to occur within a time t is :

$$F_1 = \int_0^t f_1(\lambda_1, t') \, dt' = 1 - e^{-\lambda_1 t}$$

The probability density for observing a daughter decay with a decay constant λ_2 from a parent with decay constant λ_1 is :

$$f_2(\lambda_1, \lambda_2, t) = \frac{\lambda_1 \lambda_2}{\lambda_2 - \lambda_1} (e^{-\lambda_1 t} - e^{-\lambda_2 t})$$

The probability for that daughter decay to occur within a time t is:

$$F_2(\lambda_1, \lambda_2, t) = 1 - \frac{\lambda_1 \lambda_2}{\lambda_2 - \lambda_1} (\frac{1}{\lambda_1} e^{-\lambda_1 t} - \frac{1}{\lambda_2} e^{-\lambda_2 t})$$

The probability density for observing a granddaughter decay with a decay constant λ_3 from a granddaughter with decay constant λ_2 and a parent with decay constant λ_1 is :

$$f_3(\lambda_1, \lambda_2, \lambda_3, t) = \frac{\lambda_1 \lambda_2 \lambda_3}{(\lambda_2 - \lambda_1)(\lambda_3 - \lambda_1)(\lambda_3 - \lambda_2)} \times$$
$$\left[(\lambda_3 - \lambda_2) e^{-\lambda_1 t} - (\lambda_3 - \lambda_1) e^{-\lambda_2 t} + (\lambda_2 - \lambda_1) e^{-\lambda_3 t} \right]$$

The probability for that granddaughter decay to occur within a time t is:

73

$$F_3(\lambda_1, \lambda_2, \lambda_3, t) = 1 - \frac{\lambda_1 \lambda_2 \lambda_3}{(\lambda_2 - \lambda_1)(\lambda_3 - \lambda_1)(\lambda_3 - \lambda_2)} \times$$

$$\left[\frac{(\lambda_3 - \lambda_2)}{\lambda_1} e^{-\lambda_1 t} - \frac{(\lambda_3 - \lambda_1)}{\lambda_2} e^{-\lambda_2 t} + \frac{(\lambda_2 - \lambda_1)}{\lambda_3} e^{-\lambda_3 t} \right]$$

Additionally, the probability for observing exactly r background events in a time t, given a background rate b is :

$$B_r = \frac{(bt_c)^r e^{-bt_c}}{r!}$$

4.5.4 Probability for Observing Decays

To perform the MLH analysis, the probability of actually seeing a decay must be calculated. This includes the probability for decay events to occur as shown above, as well as incorporating the efficiency of detecting the beta decays. This can be shown simply for the detection of no beta decays within a correlation time t_c. The equations for one, two, or three observed beta decays follow in the same manner but are too lengthy to be listed here. To determine the probability for detecting a beta decay, we must look at the probability that a decay from a particular generation i happens D_i, and the probability that it is observed O_i. The efficiency for detection of each generation is given by ϵ_i. The notation $\overline{F} = 1 - F \overline{\epsilon} = 1 - \epsilon$ is used, with B_o as he probability that no background events are seen in the correlation window.

The total probability to see no parent, daughter, granddaughter or background event comes from four terms: 1) that a parent does not decay, 2) that a parent decays but is not observed and the daughter does not decay, 3) that the parent decays and is not observed, the daughter decays and is not observed, and the granddaughter does not decay and 4) the parent, daughter, and granddaughter decay but are not observed.

$$P_0 = (\overline{D}_1 + D_1\overline{O}_1\overline{D}_2 + D_1\overline{O}_1D_2\overline{O}_2\overline{D}_3 + D_1\overline{O}_1D_2\overline{D}_2D_3\overline{O}_3) \times B_0$$

Plugging in the probability functions F from above and the detection efficiencies, the equation becomes:

$$P_0(\lambda_1, \lambda_2, \lambda_3, t) = [1 - F_1(\lambda_1, t)\epsilon_1 - F_2(\lambda_1, \lambda_2, t)\overline{\epsilon}_1\epsilon_2 - F_3(\lambda_1, \lambda_2, \lambda_3, t)\overline{\epsilon}_1\overline{\epsilon}_2\epsilon_3] \times B_0$$

By including the possibility that one, two, or three neutrons may be emitted after beta decay the equation for the probability becomes:

$$
\begin{aligned}
P_0(\lambda_1, \lambda_2, \lambda_3, \lambda_{2n}, \lambda_{3n}, \lambda_{3nn}, t) \ = [&1 - F_1(\lambda_1)\epsilon_1 \\
&-((1 - P_n)F_2(\lambda_1, \lambda_2) \\
&+P_nF_2(\lambda_1, \lambda_{2n}))\overline{\epsilon}_1\epsilon_2 \\
&-((1 - P_n)(1 - P_{nn})F_3(\lambda_1, \lambda_2, \lambda_3) \\
&+(1 - P_n)P_{nn}F_3(\lambda_1, \lambda_2, \lambda_{3n}) \\
&+P_n(1 - P_{n2n})F_3(\lambda_1, \lambda_2, \lambda_{3n}) \\
&+P_nP_{n2n}F_3(\lambda_1, \lambda_{2n}, \lambda_{3nn}))\overline{\epsilon}_1\overline{\epsilon}_2\epsilon_3] \times B_0
\end{aligned}
$$

4.5.5   Obtaining Background Rates From Zero-Decay Probability

For each isotope it is possible to calculate the background from the number of events where no decay was observed N_0, relative to the number of events where at least one decay was observed N_{123}.

$$\frac{N_0}{N_{123}} = \frac{P_0}{1 - P_0}$$

N_0 and N_{123} are both measured in the experiment, N_0 is the number of implants for which no decay event is seen, while N_{123} is the number of implant events for which at least one decay is seen. The background rate for r = 0 is then:

75

$$b = \frac{-\ln B_0}{t_c}$$

Using the equation for P_0, one can calculate the background rate from the number of implants seen:

$$B_0 = \frac{N_0}{N_0 + N_{123}} \times (1 - F_1\epsilon_1 - F_2\bar{\epsilon}_1\epsilon_2 - F_3\bar{\epsilon}_1\bar{\epsilon}_2\epsilon_3)^{-1}$$

4.5.6 Likelihood Function

The total likelihood function for decay events is the sum of the probability functions for seeing one, two, or three decays:

$$\mathcal{L}_{123}(\lambda_1) = \prod_{i=1}^{N_{123}} (\delta(n_i - 1)p_1 + \delta(n_i - 2)p_2 + \delta(n_i - 3)p_3)$$

The decay constant λ_1 the solution for the maximization equation:

4.6 Errors

4.6.1 Statistical Error Contributions

The reported errors include both statistical and systematic error contributions. The statistical error is obtained directly from the Maximum Likelihood analysis, which has been used before in cases of poor statistics. Because the likelihood probability density is not symmetric about the maximum, an interval was chosen such that the interval distance was the minimum to contain 68% of the area under the curve.

4.6.2 Systematic Error Contributions

The uncertainties in the half-lives and P_n values of the daughter and granddaughter as well as the N-1 daughter and granddaughter contribute to the systematic error

for the parent half-life calculation. In addition, the background and beta-detection efficiency contribute as well.

The contribution of these factors to the overall error was obtained by varying each of these parameters within their own uncertainty limits. The plus and minus one sigma values for each were used for each parameter, while the nominal values were used to determine the quoted half-life values.

4.7 Halflife Results
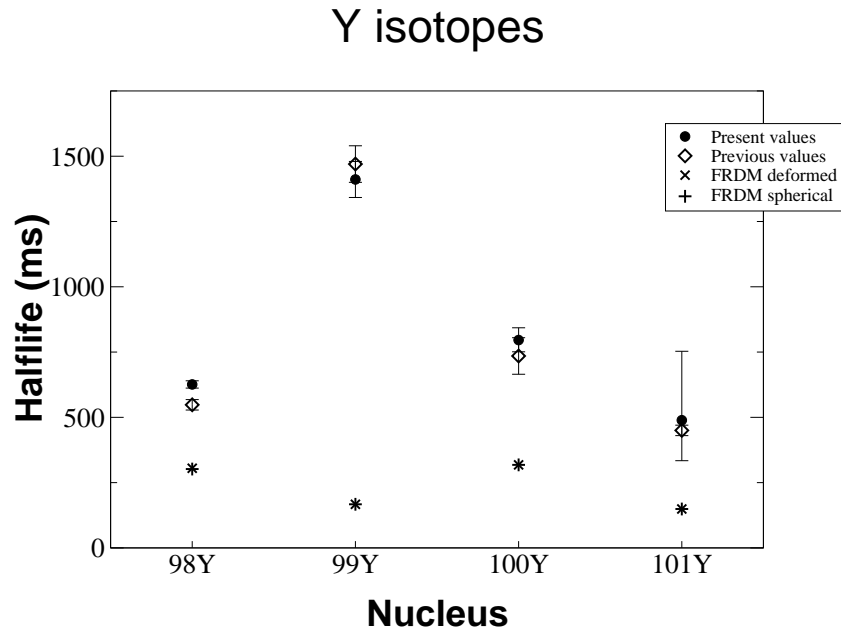

Figure 4.18. Results for Y isotopes, along with previous measurements [?] and FRDM-QRPA calculations [50]. Note that FRDM deformed and spherical resulst overlap in some cases.

Figure 4.19. Results for Sr isotopes, along with previous measurements [?] and FRDM-QRPA calculations[50].

Figure 4.20. Results for Rb isotopes, along with previous measurements [?] and FRDM-QRPA calculations[50].

Kr isotopes

Figure 4.21. Results for Kr isotopes, along with previous measurements [?] and FRDM-QRPA calculations[50].
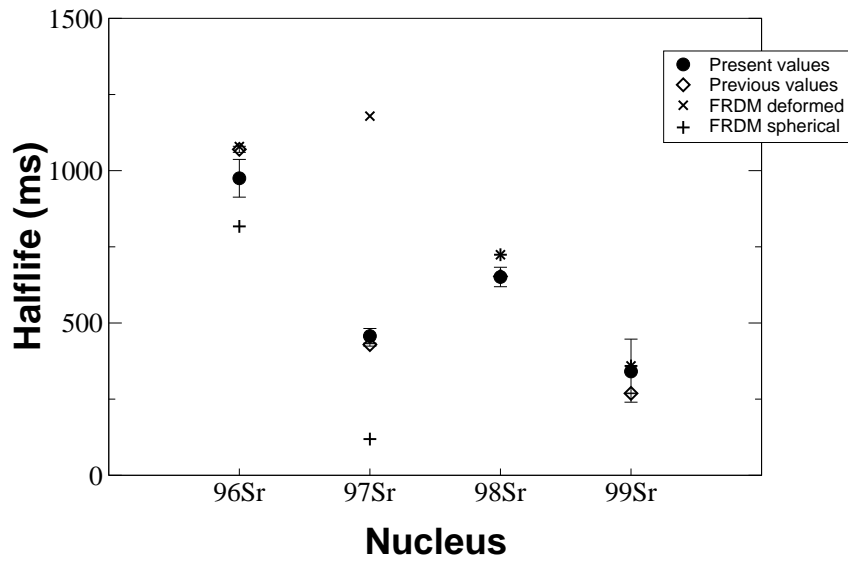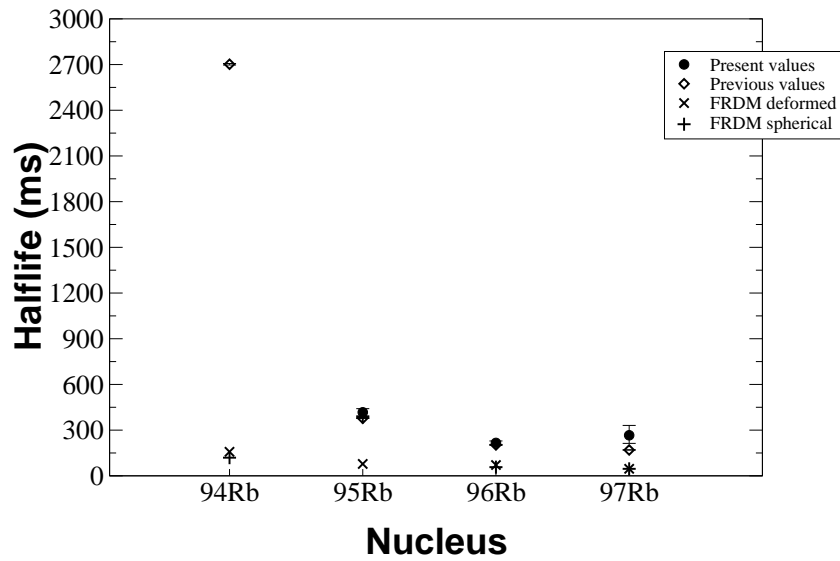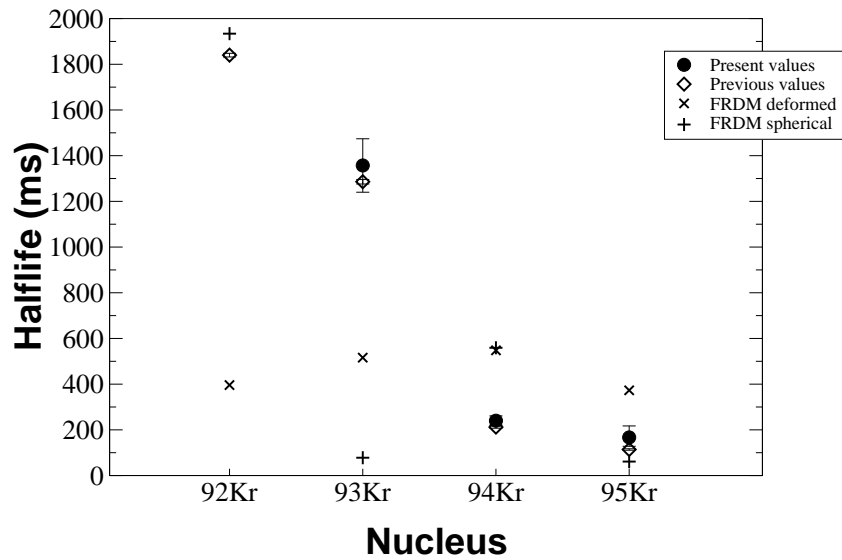
Br isotopes
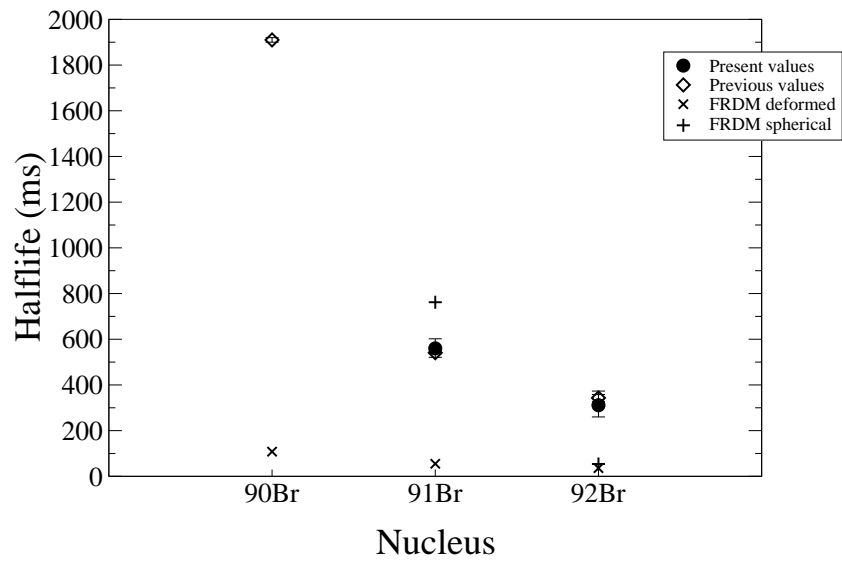
Figure 4.22. Results for Br isotopes, along with previous measurements [?] and FRDM-QRPA calculations[50].

Se isotopes
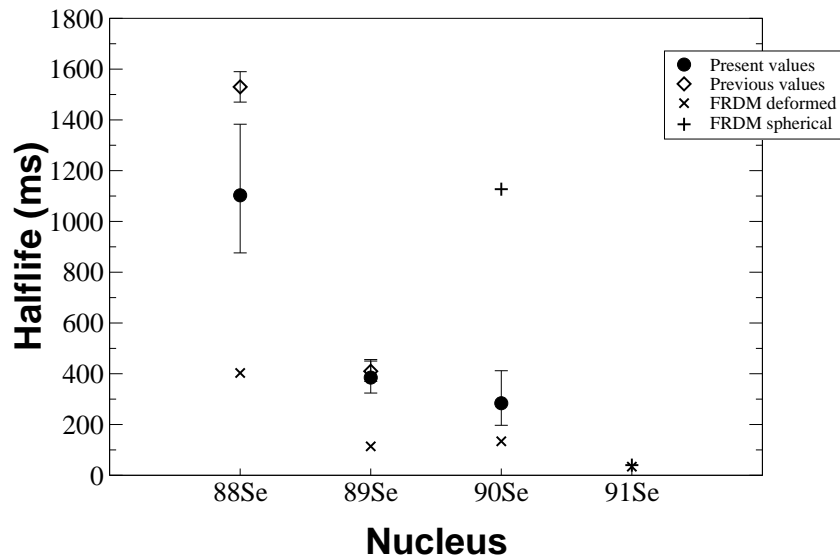
Figure 4.23. Results for Se isotopes, along with previous measurements [?] and FRDM-QRPA calculations[50].

As isotopes
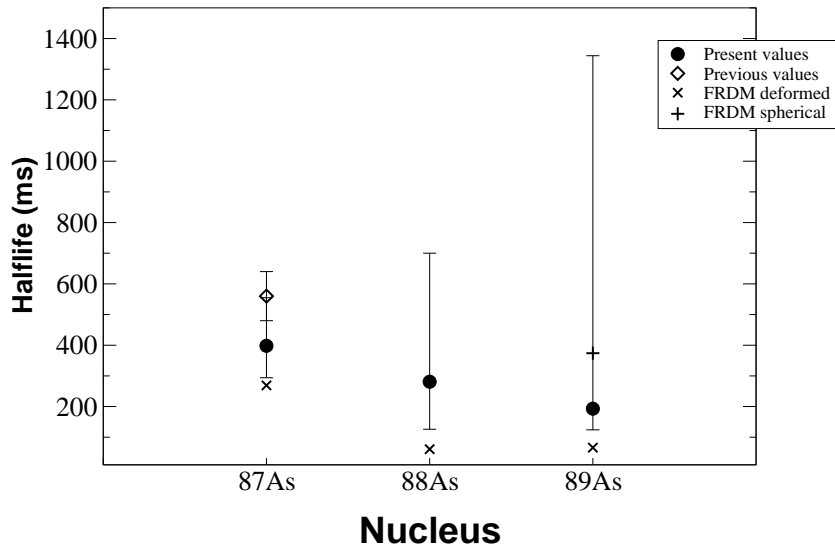
Figure 4.24. Results for As isotopes, along with previous measurements [?] and FRDM-QRPA calculations[50].
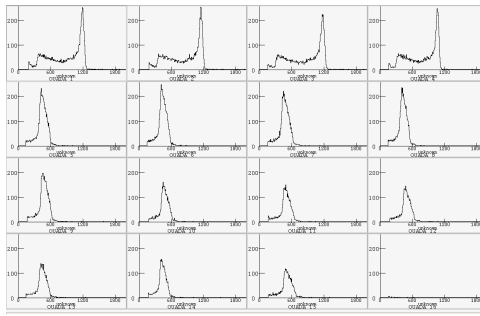
Figure 4.25. ADC spectra for NERO quadrant A. Y axis is the number of counts in each detector. X axis is the uncalibrated neutron energy. Detectors 1-4 are ^{3}He detectors, and show their characteristic spectrum, with a sharp peak at the Q value of 0.764MeV. Behind that peak are events where the entire Q value of the reaction was not deposited into the detector. When the outgoing deuterons strike the tube walls a sharp drop in the spectra can be seen. Below that, the events for which the ^{3}H nuclei strike the tube walls can also be seen. Detectors 5-15 are BF_3 detectors, which show a broader peak at the full Q value of 2.792MeV.
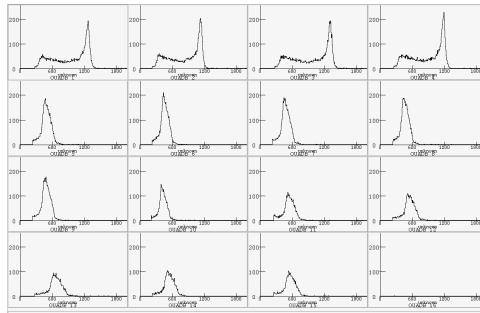
Figure 4.26. ADC spectra for NERO quadrant B.
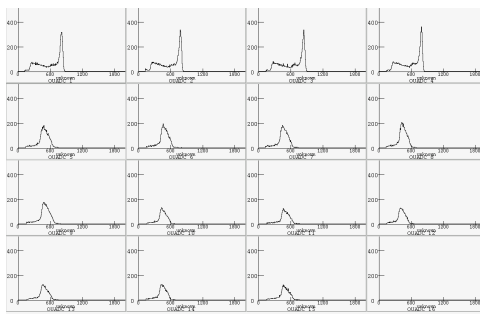
Figure 4.27. ADC spectra for NERO quadrant C.
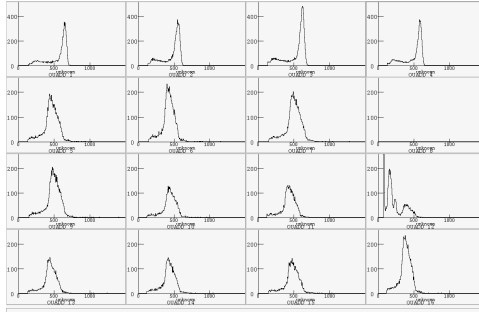
Figure 4.28. ADC spectra for NERO quadrant D.
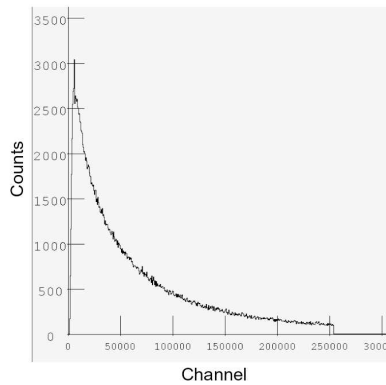
Figure 4.29. TDC spectrum from NERO ring 1 detectors. Channels are proportional to time neutron is detected after a beta decay event. Ring 1 is the innermost ring of detectors, and therefore sees more neutrons shortly after beta decay with relatively few neutrons coming at later times.
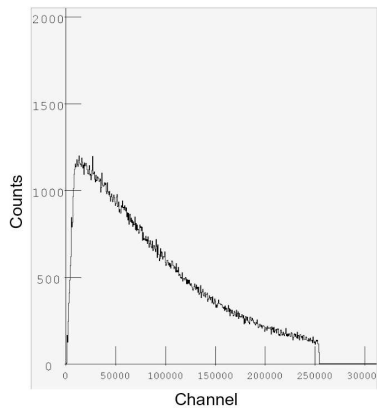
Figure 4.30. TDC spectrum from NERO ring 2 detectors. Channels are proportional to time neutron is detected after a beta decay event. Ring 2 is the middle ring of detectors, and sees more neutrons at later times than does ring 1. This is due to the fact that neutrons reaching this ring have to travel through more moderating material.
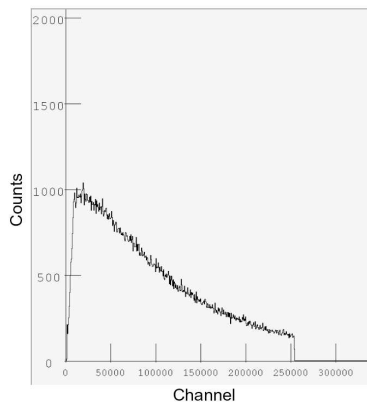
Figure 4.31. TDC spectrum from NERO ring 3 detectors. Channels are proportional to time neutron is detected after a beta decay event. Ring 3 is the outermost ring of detectors, and sees the most neutrons at later times of all the NERO rings.
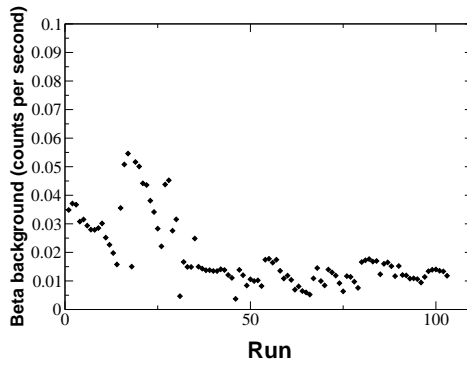
Figure 4.32. β background rate versus run number.
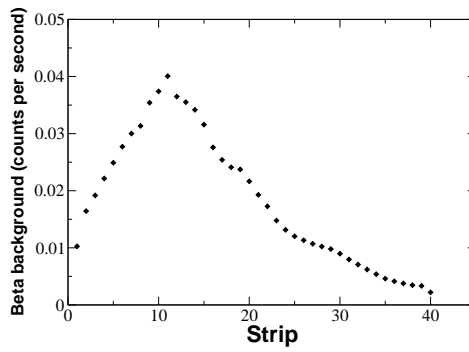
Figure 4.33. β background rate versus DSSD front strip number.
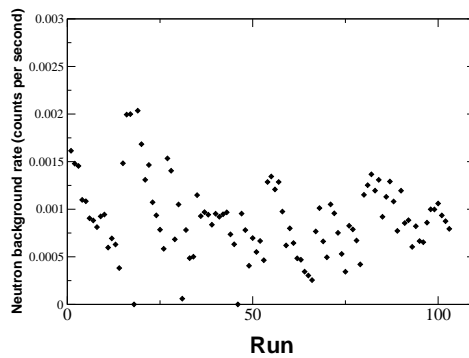
Figure 4.34. Neutron background rate versus run number.

84
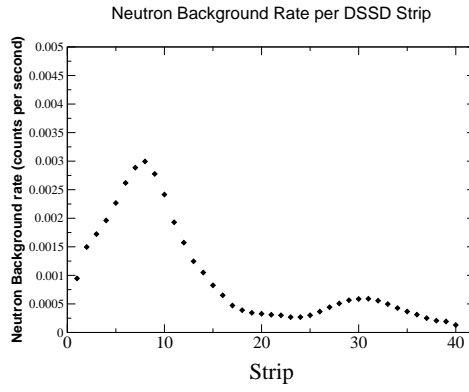
Figure 4.35. Neutron background rate versus DSSD front strip number.
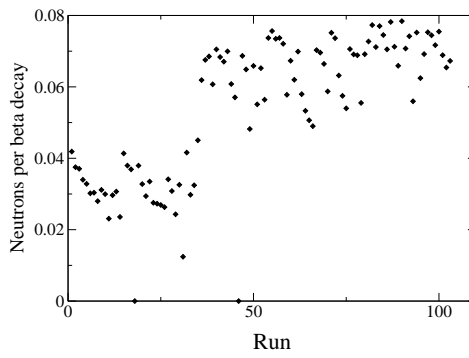
Figure 4.36. Background neutrons per β as a function of run number.

85

TABLE 4.1

PREVIOUS HALFLIFE MEASUREMENTS

	Present Work	Previous	Theory	
Nucleus	$T_{1/2}(ms)$	$NNDCT_{1/2}(ms)$	FRDM Def(ms)	FRDM Sph(ms)[50]
^{87}As	$0.398_{0.104}^{0.157}$	0.5600(0.08)	0.269	2.458
^{88}As	$0.281_{0.155}^{0.419}$		0.061	2.263
^{89}As	$0.193_{0.069}^{1.151}$		0.066	0.374
^{88}Se	$1.103_{0.227}^{0.280}$	1.5300(0.06)	0.403	12.312
^{89}Se	$0.385_{0.061}^{0.071}$	0.4100(0.04)	0.114	9.050
^{90}Se	$0.284_{0.087}^{0.128}$		0.134	1.127
^{91}Br	$0.560_{0.039}^{0.042}$	0.5410(0.005)	0.055	0.762
^{92}Br	$0.311_{0.051}^{0.062}$	0.3430(0.015)	0.036	0.054
^{93}Kr	$1.357_{0.117}^{0.117}$	1.2860(0.01)	0.516	0.078
^{94}Kr	$0.240_{0.019}^{0.021}$	0.2120(0.005)	0.548	0.559
^{95}Kr	$0.167_{0.039}^{0.050}$	0.1140(0.003)	0.373	0.061
^{95}Rb	$0.417_{0.023}^{0.024}$	0.3775(0.0008)	0.078	0.386
^{96}Rb	$0.216_{0.012}^{0.013}$	0.2028(0.0033)	0.071	0.057
^{97}Rb	$0.266_{0.053}^{0.065}$	0.1699(0.0007)	0.046	0.046
^{96}Sr	$0.975_{0.062}^{0.062}$	1.0700(0.01)	1.079	0.817
^{97}Sr	$0.457_{0.025}^{0.025}$	0.4290(0.005)	1.179	0.119
^{98}Sr	$0.651_{0.032}^{0.032}$	0.6530(0.002)	0.724	0.724
^{99}Sr	$0.341_{0.101}^{0.106}$	0.2690(0.001)	0.359	0.359
^{98}Y	$0.626_{0.014}^{0.014}$	0.5480(0.002)	0.305	0.302
^{99}Y	$1.411_{0.069}^{0.069}$	1.4700(0.007)	0.167	0.167
^{100}Y	$0.796_{0.045}^{0.047}$	0.7350(0.007)	0.318	0.318
^{101}Y	$0.489_{0.155}^{0.264}$	0.4500(0.02)	0.149	0.149

## 4.8 Neutron Analysis

4.8.1 Neutron Events

NERO was allowed to count neutrons after a high-gain (beta) DSSD event. This was done by opening a gate for $200\mu s$ after any such event. The neutron energy signal was recorded via an ADC, and the neutron time was recorded by a TDC. The ADC only recorded the first neutron event during the $200\mu s$ window, while the

TDC recorded all events. The individual ADC spectra and TDC spectra for each ring are shown below.

4.8.2 Calculating P_n values

Obtaining the P_n value for a particular nucleus begins with the equation:

$$P_n = 100 \times \frac{N_{\beta-n}}{N_{\beta parent}}$$

This equation states that the P_n value (in %) is the number of beta-delayed neutrons detected divided by the number of parent nucleus beta decays. Because the beta decays detected could be from the parent, daughter, granddaughter, or background, we must calculate the number of parent beta decays that should be detected. $N_{\beta parent}$ is the number of parent nucleus beta decays, and is calculated from the total number of beta decays for a particular nucleus by:

$$N_{\beta parent} = N_{imp}(1 - e^{-\lambda t_{corr}})$$

where λ is the decay constant of the parent nucleus, and t_{corr} is the correlation time for beta decay events (either 5 or 10 seconds). N_{imp} is the total number of implants for that particular nucleus.

The number of beta-delayed neutrons detected $N_{\beta n-detected}$ must be corrected for the efficiency of NERO and the BCS, as well as for the neutron background observed. Thus, $N_{\beta-n}$ is given by:

$$N_{\beta-n} = \frac{N_{\beta n-detected} - N_{\beta n-background}}{\epsilon_{\beta n}}$$

where $N_{\beta n-detected}$ is the raw number of beta-delayed neutrons detected, $N_{\beta n-background}$ is the number of background beta-delayed neutrons detected in the correlation window, and $\epsilon_{\beta n}$ is the total efficiency for detecting beta-delayed neutrons. $\epsilon_{\beta n}$ is given by: $\epsilon_{\beta n} = \epsilon_{NERO}\epsilon_{\beta}$ where ϵ_{NERO} is the detection efficiency of NERO, and ϵ_{β} is the

detection efficiency of the BCS. The number of beta-delayed neutrons detected in the correlation window after an implant $N_{\beta n-background}$ is calculated by the equation:

$$N_{\beta n-background} = Rate_{\beta n} \times t_{corr} \times N_{imp}$$

where t_{corr} is the correlation window of 5 or 10 seconds, N_{imp} is the number of implants of a particular nucleus, and $Rate_{\beta n}$ is the per pixel neutron background averaged over each run.

4.9 P_n Results

TABLE 4.2

PREVIOUS P_n MEASUREMENTS

	Present Work	Previous	Theory	
Nucleus	Pn(%)	Previous value(%)	FRDM Def(%)	FRDM Sph(%)[50]
90Br	23.6(1.7)	25.2(9.0)	1.818	99.800
91Br	14.6(2.0)	20(3)	3.319	73.365
92Br	40.9(5.0)	33.1(21.0)	13.032	8.458
94Rb	7.3(0.4)	10.01(0.23)	1.414	1.628
96Rb	6.5(2.2)	13.4(0.4)	10.634	10.546

CHAPTER 5

DISCUSSION

5.1 Half-life Calculations

The evolution of shell structure away from the line of stability is a major open question in nuclear physics. The results of shell gaps disappearing or new gaps appearing, affect our understanding of the nucleus and of stellar processes like the r-process. While not a direct measure of the shape of a nucleus, the beta decay halflife can give insight into the nuclear shape, and the evolution of shape in a region of the chart of the nuclides.

The present results have been compared to QRPA halflife calculations using the FRDM mass model. QRPA calculations are able to provide information on a wide range of nuclei far from the line of stability, and have been used previously in r-process calculations. The calculation begins by computing the ground state nuclear masses and deformations with the FRDM. The FRDM, or Finite Range Droplet Model, is a macroscopic-microscopic type model that calculates the total potential energy of the nucleus. It treats the nucleus as a liquid drop, but also takes into account the effect on the surface energy due to the finite range of the nucleon-nucleon interaction. Additionally, it treats the effect of nuclear shape on the Coulomb field and the diffusness of the charge distribution, and introduces a exponential compressability term that corrects earlier drop models' tendencies to overstate the central nuclear density. Microscopically it includes a three part

potential for use in the Strutinski integral in order to introduce shell corrections, and the Lipkin-Nogami version of the BCS method for pairing corrections.

The potential energy surface of the nucleus is calculated as a function of the quadrupole deformation ϵ_2 and octapole deformation ϵ_4. The ground state deformation of a nucleus is determined by finding the minimum in this potential energy surface. With the deformations determined, values that depend on the shape of the nucleus such as the mass and fission barriers can be calculated.

With the ground state shapes and masses determined, a quasi random phase approximation (QRPA) calculation is then done to obtain the beta decay halflives and P_n values. This is done by adding a Gamow-Teller force of the form:

$$V_{GT} = 2\chi_{GT}\beta^{1-}\beta^{1+}$$

to the folded-Yukawa Hamiltonian, where:

$$\beta^{1\pm} = \Sigma_i \sigma_i t_i^{\pm}$$

The beta decay halflife is obtained from the beta strength function, which is the square of the nuclear matrix element. Therefore:

$$S_\beta \propto \langle \phi_f | V_{GT} | \phi_i \rangle^2$$

The halflife is then:

$$\frac{1}{T_{1/2}} = \sum_{E_i}^{Q_\beta} S_\beta(E_i) \times f(Z, Q_\beta - E_i)$$

where Q_β is the Q value of the beta decay, $E_i = Q_\beta - E_0$ is the excitation energy in the daughter nucleus, and $f(Z, Q_\beta - E_i)$ is the Fermi function, which is proportional to $(Q_\beta - E_i)^5$.

The beta delayed neutron emission ratio can be calculated by looking at the ratio of the beta strength above the neutron separation energy S_n to the total beta strength.

$$P_n = \frac{\sum_{S_n}^{Q_\beta} S_\beta(E_i) \times f(Z, Q_\beta - E_i)}{\sum_0^{Q_\beta} S_\beta(E_i) \times f(Z, Q_\beta - E_i)}$$

5.1.1 Comparison to Data

The results of this experiment are compared with QRPA calculations and with previous results in Figs 5.1 and 5.2. There is generally good agreement with previously measured values, with the possible exception of ^{98}Y and ^{100}Y. These nuclei have low-lying states from which beta decay is possible. Because we can not separate these states, the observed halflives are superpositions of these two states.

For the Se and As nuclei, there is good agreement with the QRPA deformed calculations. The half-lives are slightly larger than the predicted values, but the overall trend is consistent, and the predicted values for spherical shapes are much higher.

Se isotopes
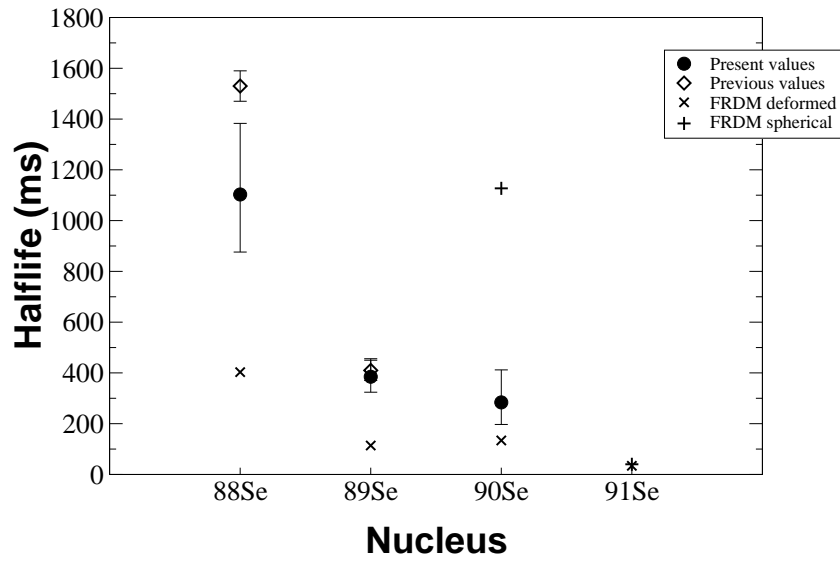
Figure 5.1. Se isotopes results compared with FRDM predictions.

As isotopes
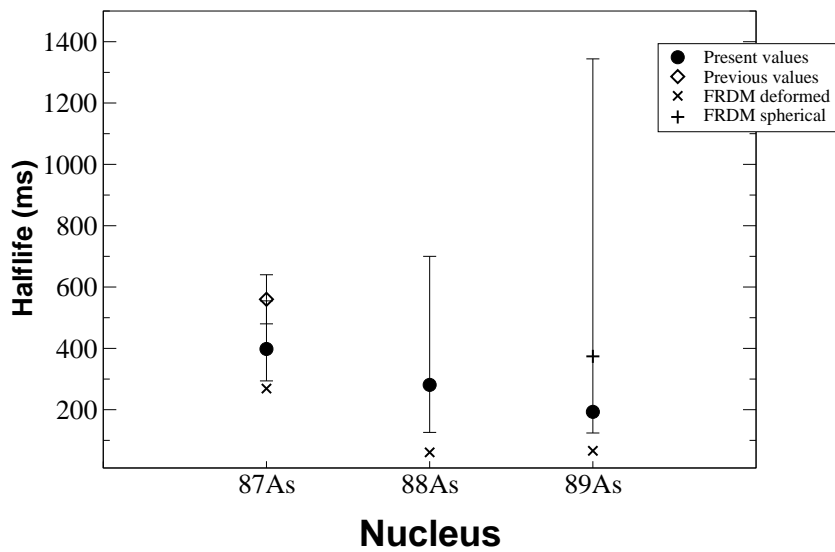
Figure 5.2. As isotopes results compared with FRDM predictions.

5.2 Deformation Discussion

The agreement of the measured beta decay halflife with the FRDM-QRPA predictions for a deformed shape, as opposed to a spherical shape agrees with predictions for the ground state deformation[44],[45]. The deformed ground state shape is predicted because of a shell gap at $Z = 34$ due to the splitting of the $1_{f5/2}$ orbitals. The $E(2^+)$ systematics for the Se isotopes are unclear as N approaches 56, as can be seen in Fig 5.3. Generally, the first 2^+ state in a spherical nucleus will be at a higher energy than for deformed nuclei. Looking at Fig 5.7, one can pick out the high $E(2^+)$ for the $N = 50$ closed shell. The trend past $N = 50$ looks as though the $E(2^+)$ at $N = 56$ could either increase to over 1MeV, which would indicate a spherical shape; or may decrease to below 800 keV, which would indicate a more deformed shape.
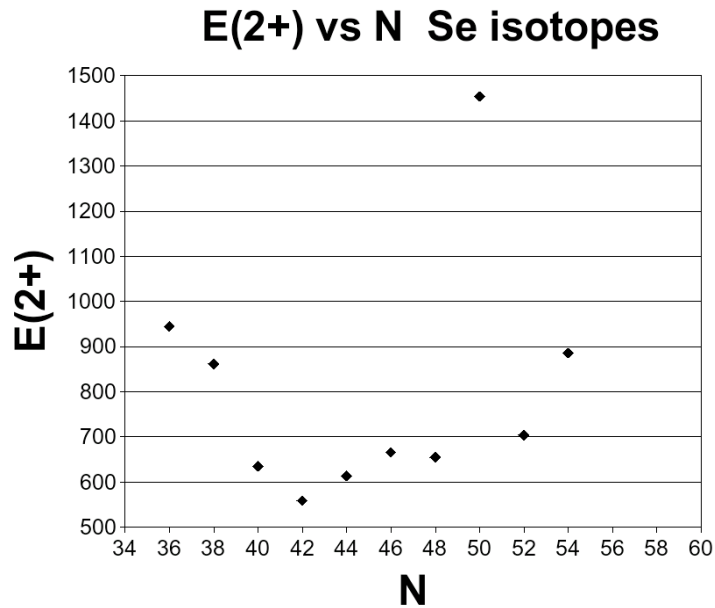
Figure 5.3. Measured $E(2^+)$ values for Se isotopes.
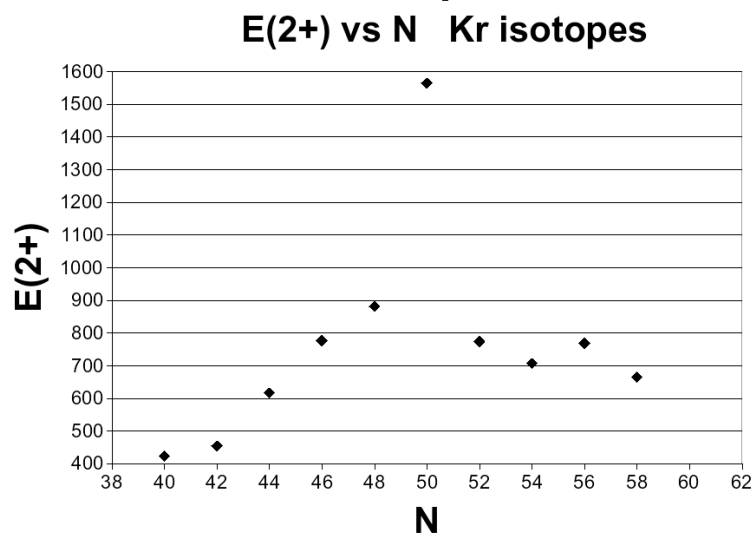
Figure 5.4. Measured $E(2^+)$ values for Kr isotopes.
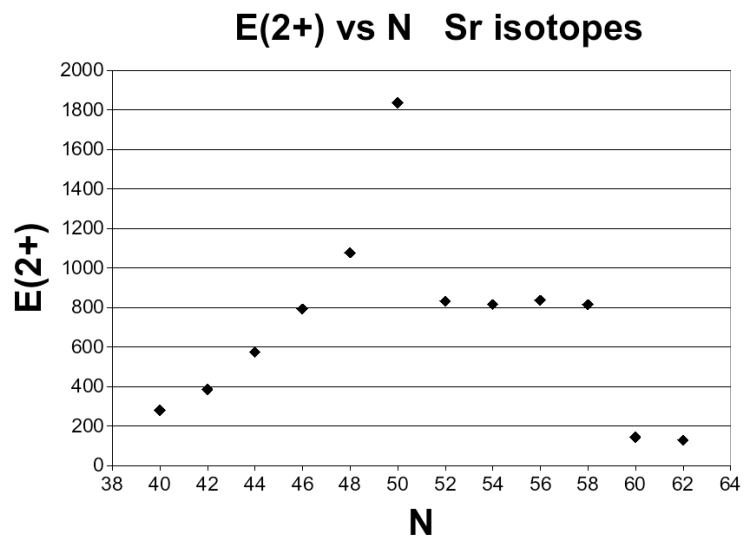
Figure 5.5. Measured $E(2^+)$ values for Sr isotopes.

The suggestion of $N = 56$ as a spherical sub shell closure comes largely from the case of ^{96}Zr, which has a large $E(2^+)$ value. The trend of the $N = 56$ isotones suggests shell closures at $Z = 40$ and 50 but not away from those nuclei(Fig 5.7). The suggested means for creating the $N = 56$ subshell closure is by the lowering of the $\nu 2_{d5/2}$ level, which can hold six neutrons. ^{94}Sr nucleus (Fig 5.5).

Based on the $N = 56$ systematics, a spherical shape for the ground state of ^{94}Sr would require that $Z = 34$ be shell closure as well. There are predictions of a $N = 34$ subshell closure around $Z = 20$ [?], however experimental evidence [?] does not support such a closure. The proposed mechanism for the emergence of this subshell closure is the lowering of the $2_{p1/2}$ below the $1_{f5/2}$ due to a weaker monopole interaction[46]. Even if a similar closure were to exist for $Z = 34$, it seems unlikely that the $\pi 2_{p1/2}$ and $\pi 2_{p3/2}$ states would strongly interact with the $\nu 2_{d5/2}$ state necessary to create the $N = 56$ closure because of the large difference in spin-orbit coupling ($\frac{1}{2}$ vs $\frac{5}{2}$).
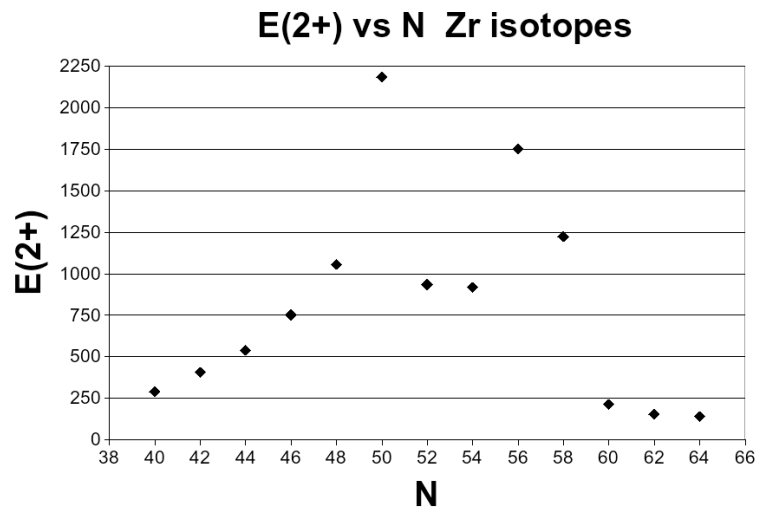
Figure 5.6. Measured $E(2^+)$ values for Zr isotopes.
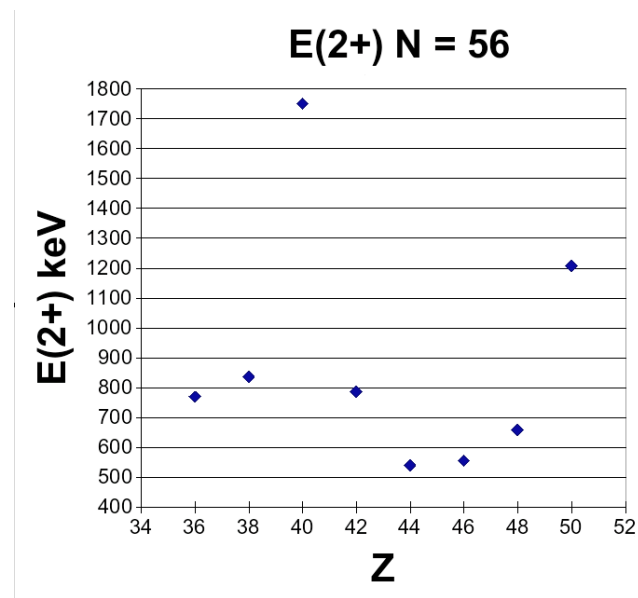
Figure 5.7. Measured $E(2^+)$ values for $N = 56$ isotones.

5.3 R-Process Calculations

In order to investigate the impact of these measurements on the r-process, the measured halflives and P_n values were put into a classical r-process simulation code. This code starts with a ^{56}Fe seed and uses the assumption of a

$$(n, \gamma) \rightleftharpoons (\gamma, n)$$

equilibrium to calculate the isotopic abundances for each element. The isotopic abundances are determined by the Saha equation, so that the neutron number density N_n, the neutron separation energy S_n, an the temperature T largely determine the waiting point nuclei.

$$\frac{Y(Z, A+1)}{Y(Z, A)} = N_n \frac{G(Z, A+1)}{G(Z, A)} \left(\frac{A+1}{A}\right)^{3/2}$$

$$\times \left(\frac{2\pi\hbar^2}{m_u kT}\right)^{3/2} e^{\frac{S_n(Z, A+1)}{kT}}$$

Where G are the partition functions. The abundance for each element is then:

$$Y(Z) = \sum_A Y(Z, A)$$

. Once the abundances for each isotopic chain are calculated, the flow from one element to the next can be calculated via:

$$\frac{dY(Z, A)}{dt} = Y(Z-1, A)(1 - P_n^{(Z-1,A)})\lambda_\beta^{(Z-1,A)}$$

$$+Y(Z-1, A+1)P_n^{(Z-1,A+1)}\lambda_\beta^{(Z-1,A+1)} - Y(Z, A)\lambda_\beta^{(Z,A)}$$

After a process time t freeze-out occurs, and only β decays are considered, until the nuclei have decayed back to stability. After freeze-out occurs, beta-delayed neutron emission may occur and change the final abundance distribution.

5.3.1 R-Process results

A simulation using the present experimental results is shown in Fig 5.8 along with the observed solar system r-process abundances. Also shown are the r-process abundances for the FRDM-QRPA predictions for spherical Se nuclei. The simulation was done with three neutron exposures of:

TABLE 5.1

ASTROPHYSICAL PARAMETERS USED FOR R-PROCESS SIMULATION

N_n	Temperature (GK)	Time (s)	Weighting
1×10^{20}	1.35	2000	9.2
5×10^{22}	1.35	1800	1.0
1.5×10^{25}	1.35	1650	0.75

The results show that the halflife of ^{90}Se has a strong effect on the abundances of the nuclei up to the A = 130 peak. The difference between a spherical and deformed shape for this nucleus changes the abundances by a factor of two. The measured halflife of 284ms for ^{90}Se produces more material for A = 90 -130 than does the spherical prediction of 1127ms. These results agree with previous predictions of more r-process material due to shorter beta-decay halflives[47].

Longer half-lives in a region generally result in *more* r-process abundance for that region. Longer halflives at the waiting points is the reason that the nuclei at or near closed shells (such as N = 82, 126) have larger r-process abundances. Results were qualitatively similar for several different mass models.

From the simulations, it is clear that the *Se* isotopes have a larger effect on the r-process at low neutron number densities. The exposure of $N_n = 10^{20}$ was the only one to be greatly effected by the variation in *Se* halflives. Because of this
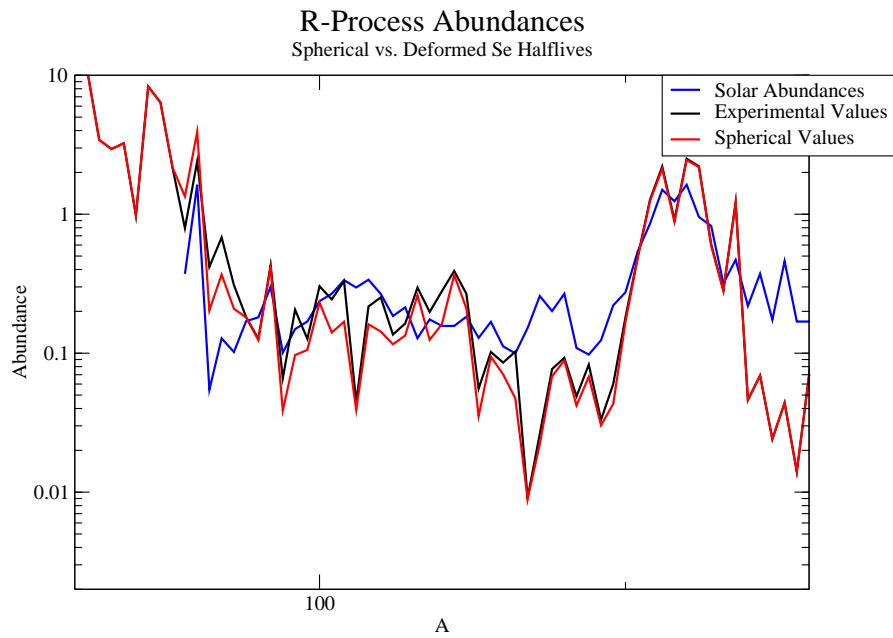
Figure 5.8. Results of R-Process simulation using measured half-life values (black line) and values predicted for spherical ground state shapes (red line).

importance to lower values of N_n, the question of a weak r-process or other neutron capture process may be of concern. It was seen that neutron number densities of between 10^{18} and 10^{21} can be affected by the halflives in this region. At $N_n = 10^{16}$ though, the change in halflives did not strongly affect the final abundances.

CHAPTER 6

CONCLUSION

The goal of this work was to provide a better understanding of the mechanisms that are responsible for creating the matter that makes up our solar system, and the world around us. This knowledge has been sought by civilizations across the world for thousands of years. However, it has only been within the last century that we have approached a scientific understanding of the origin of the elements. The connection between nuclear fusion and stellar fuel was first made by Arthur Eddington in 1920 and extended by George Gamow, and Hans Bethe (among many others). They realized that the energy provided by the fusion of hydrogen into helium could provide enough energy to counteract the gravitational contraction of stellar material. This link was the first step to explaining how heavier elements are made.

We know that after the Big Bang mostly hydrogen and helium nuclei were present. It was not until the first generation of stars began to convert hydrogen into helium that the nuclear abundances changed. The p-p chains and CNO cycle account for conversion of hydrogen into helium. Helium is converted into carbon through the triple-alpha reaction, while oxygen and neon are created by the burning of helium and carbon. Further nuclear burning can produce nuclei as heavy as iron. Carbon, oxygen, neon, and silicon burn until iron group nuclei are produced. Because these nuclei have the highest binding energies per nucleon, heavier nuclei

are generally not produced by charged particle reactions. In some cases though, the rapid proton capture process can create elements heavier than iron.

To make nuclei heavier than iron, reactions involving uncharged neutrons are required. Nuclei of any Z can capture neutrons, so we know that elements beyond iron must be created through neutron reactions. The shape of the elemental abundance curve provides some clues about how different processes contribute to the total abundances. The abundance curve is dominated by three sets of double peaks past the iron region. These double peaks seem to indicate two separate processes driven by similar physics. These two processes are known as the slow (s) and rapid (r) neutron capture processes.

Currently, the reason for two sets of peaks is thought to be that they are the s and r processes reaching neutron shell closures at different points. The s-process moves along closer to the line of nuclear stability, and therefore has a greater number of protons at each neutron shell closure. The r-process path is further from stability which means that it will have fewer protons at each neutron shell closure. A nucleus in the r-process will capture several neutrons, until the point where any additional neutrons will be emitted as soon as they are captured. This nucleus, known as a waiting point nucleus will beta decay to its daughter (with Z+1). Thus the β decay rate is extremely important in determining the final abundances from the r-process. Longer β decay halflives at particular waiting points will result in greater nuclear abundance around those waiting points, with reduced abundance beyond. Shorter halflives will result in a quicker r-process and greater abundance of the heaviest nuclei. In addition, the beta-delayed neutron emission ratio P_n is also very important to determining the final nuclear abundances from the r-process. After the process ends and nuclei begin to beta decay back to stability, beta- delayed neutron emission will change the mass A of nuclei.

Because of the importance of β decay halflives and P_n values to the r-process, it was the aim of this work to measure the β decay halflives P_n values of several r-process nuclei. The isotopes chosen were just below $Z = 40$ near $N = 60$ and include: Y, Sr, Rb, Kr, Br, Se, and As isotopes. These nuclei are interesting because they lie in the r-process path and are near ^{100}Zr, which is characterized by its unexpected ground state deformation. With the addition of only a few neutrons, Zr goes from a spherical shape to a deformed shape. This change in shape also produces a sharp increase in the beta-decay halflife. The nuclei we sought to measure might also have such a rapid change in shape, but a corresponding change in the halflife and Pn value would have consequences for the r-process. The nucleus ^{90}Se in particular is interesting because it has $N = 56$ like the spherical nucleus ^{96}Zr. There are predictions that it too might have a spherical shape and a longer half-life. A computer simulation shows that show that if the neutron rich Se isotopes were spherical in shape, that the r-process abundances between $A = 90 - 130$ would be lowered by a factor of two.

In this work, the beta decay halflives were measured and P_n values were calculated for neutron rich isotopes below $Z = 40$ produced at the NSCL coupled cyclotron facility at Michigan State University. Because these nuclei are so far from stability, they are extremely difficult to produce. The NSCL is one of only a few facilities around the world that can produce nuclei so far from stability. To measure the properties of these rare nuclei a system of silicon, germanium, and scintillator detectors was needed. Determining the halflives was done by a χ^2 minimization for the nuclei with enough counts to allow binning. For the nuclei with too few counts for this procedure to work, the Maximum Likelihood Method was used. This method has been used in other low count experiments, including similar experiments at the NSCL.

Twenty-two halflives were determined in our measurments. Three nuclei, ^{90}Se, ^{88}As, and ^{89}As, were measured for the first time. In addition, we have confirmed previously measured half-lives for Y, Sr, Rb, Kr, Br, Se, and As isotopes. The new measurements were used to calculate the P_n values for $^{92-90}$Br and ^{96,94}Rb shown in Table 4-2.

Beta decay halflives are a good first indication of nuclear structure. As stated above, ^{90}Se is a good testing ground for the strength of the $N = 56$ subshell. Based on FRDM-QRPA calculations for the halflives depending on the nuclear shape, our results suggest that ^{90}Se is deformed in shape. This agrees with predictions for the ground state shape based on a $Z = 34$ deformed shell gap. However, this refutes the concept of an $N = 56$ subshell closure below $Z = 40$. Ultimately, more measurements are needed to confirm this indication.

Using a ^{56}Fe, three different neutron exposures, and with the assumption of a $(n, \gamma) \rightleftharpoons (\gamma, n)$ equilibrium, r-process abundances have been calculated. As stated above, the results show that if the neutron rich Se isotopes were spherical in shape, that the r-process abundances between A = 90-130 would be lowered by a factor of two. Because of their importance in neutron exposures with $N_n \leq 10^{21}$, the isotopes in this region may be important for the weak r-process and other proposed neutron captures such as the LEPP. With the measurement of ^{90}Se in particular, it is possible to set new limits on the end points of processes such as the alpha-rich freezeout or the LEPP. The two possible shapes of ^{90}Se added a factor of two uncertainty in the production values in this region.

Many of the nuclei that were measured in this work have been measured previously, often with greater precision. The reason for this has to do with the methods of production in this experiment versus the previous experiments. In previous work, the method known as ion separation on line (ISOL) was used. This method pro-

duces nuclei far from stability as fission products from a thick target. The products are then extracted from the target and reaccelerates them to be stopped in a detector system. ISOL works very well for some nuclei, as can be seen in the previous measurements. This method has two large drawbacks though. The first is that the nuclei of interest must be fission products of the target. The fragment mass distributions for most fissioning nuclei are peaked at A = 90 and A = 140. Away from these masses the fission yeilds drop off sharply. This means that attempting to produce nuclei with masses much different from these values is extremely difficult. In addition to the limits of production, ISOL must also extract the product nuclei from the target and reaccelerate them. Because of the chemistry involved, some isotopes are difficult to extract at all. More importantly, this process takes time, which means that very short lived nuclei can not be extracted and reaccelerated before they decay.

These limitations mean that, especially for r-process studies, fragment separation is the method of the future. As can be seen from this work's region of interest, many of the nuclei were first produced twenty or thirty years ago, with little progress since then. This work was the first study in this area using the method that will eventually take us beyond even the r-process nuclei. Despite having production rates well below what were estimated, this experiment was able to produce new nuclei beyond what the more mature ISOL techinque has been able to. There is no inherant reason that fragmentation cannot deliver nuclei in this region and beyond in much greater quantities. Using the knowledge gained from this experiment, future experiments can optimize magnet settings and make even greater discoveries. The history of r-process experiments has been a slow and steady one. This work has delivered new results, and has laid the foundation for future discoveries.

While we have a general idea of how the heavy elements are made, we do not

know the specific details in either the nuclear structure side or the astrophysics side. There have been very few r-process nuclei produced and measured. We currently rely on models of nuclear properties to make predictions about the r-process abundances. Unfortunately it is not easy to extrapolate nuclear structure properties to nuclei far from stability. New shell closures can open, while known shell closures can disappear as extra neutrons are added. The fact that the r-process exists far from stability makes it exciting to study. However the extreme neutron excesses of the r-process means that it is difficult to produce and measure the properties of r-process nuclei.

The future will provide many more answers to the questions of heavy element creation. Today, only about ten percent of the nuclei thought possible to exist have been studied at all. Most of these unknown nuclei are extremely neutron rich. This work has extended the understanding of a section of the neutron rich nuclei involved in the r-process. Further study at current facilities will provide additional understanding of these nuclei, however an upgrade in accelerator facilities is needed to obtain experimental information about all r-process nuclei. The current plan for the Facility for Rare Isotope Beams (FRIB) will be able to produce neutron rich nuclei via projectile fragmentation with sufficient intensities to study nearly all the r-process nuclei. While the future is bright for the study of the r-process, it is critical that new facilities are built, in order to continue to answer the questions about how the elements around us are created.

BIBLIOGRAPHY

[1] W.A. Fowler, E.M. Burbidge, G. R. Burbidge, and F. Hoyle Synthesis of the Elements in Stars. *Rev. Mod. Phys.*, 29(4):547–650, 1957.

[2] National Research Council of the National Academies Connecting Quarks with the Cosmos: Eleven Science Questions for the New Century The National Academies Press, Washington, D.C., 2003.

[3] G. Lemaitre Expansion of the Universe. *Monthly Notices of the Royal Astronomical Society*, 91:490-501, 1931.

[4] E. Hubble A Relation Between Distance and Radial Velocity Among Extragalactic Nebulae. *PNAS*, 15(3):168-173, 1929.

[5] A. A. Penzias and R. W. Wilson A Measurement of Excess Antenna Temperature at 4080 Mc/s. *ApJ.*, 142(1):419, 1965.

[6] Claus E. Rolfs and William S. Rodney Cauldrons in the Cosmos. The University of Chicago Press, Chicago, Illinois, 1988.

[7] Aage Bohr and Ben R. Mottelson Nuclear Structure W.A. Benjamin, Reading, Massachusetts, 1975.

[8] M. Arnould and S. Goriely The P-Process of Stellar Nucleosynthesis. *Phys. Rep.*, 384(1):1-84, 2003.

[9] M. Busso, R. Gallino, and G.J. Wasserburg Nucleosynthesis in Asymptotic Giant Branch Stars. *Ann. Rev. Astron. Astrophys.*, 37(1):239-309, 1999.

[10] F Kappeler, H Beer, and K Wisshak S-process Nucleosynthesis-Nuclear Physics and the Classical Model. *Rep. Prog. Phys.*, 52: 945-1013, 1989.

[11] S. Goriely Uncertainties in the Solar System R-abundance Distribution. *Astron. Astophys.*, 342:881-891, 1999.

[12] S.G. Ryan, J.E. Norris, and T.C. Beers Extremely Metal-poor Stars. II. Elemental Abundances and the Early Chemical Enrichment of the Galaxy. *ApJ.*, 471(1):254-278, 1996.

[13] C. Sneden et. al The Extremely Metal-poor, Neutron Capture α rich Star CS 22892-052: A Comprehensive Abundance Analysis. *ApJ.*, 591(2):936-953, 2003.

[14] F. Montes, et. al Nucleosynthesis in the Early Galaxy. *ApJ.*, 671(2):1685-1695, 2007.

[15] G.J. Wasserburg, M. Busso, and R. Gallino Abundances of Actinides and Short-lived Nonactinides in the Interstellar Medium: Diverse Supernova Sources for the r-Processes. *ApJ.*, 466(2):109-113, 1996.

[16] D.D. Clayton, W.A Fowler, T.E Hull, and B.A Zimmerman Neutron Capture Chains in Heavy Element Synthesis. *Annals of Physics*, 12(3):331-408, 1961.

[17] P.A. Seeger, W.A. Fowler, and D.D. Clayton Nucleosynthesis of Heavy Elements by Neutron Capture. *ApJS.*, 11(1):121, 1965.

[18] K.L. Kratz Nucear Physics Constraints to Bring the Astrophysical R-Process to the Waiting Point. *Reviews in Modern Astronomy*, 1(1):184-209, 1988.

[19] A.G.W. Cameron, J.J. Cowan, H.V. Klapdor, J. Metzinger, T. Oda, and J.W. Truran Steady Flow Approximations to the Helium R-Process. *ApSS.*, 91(1):221-234, 1982.

[20] S.E. Woosley, and E. Baron The Collapse of White Dwarfs to Neutron Stars. *ApJ.*, 391(1):228-235, 1992.

[21] B.S. Meyer et al. R-Process Nucleosynthesis in the High-Entropy Supernova Bubble. *ApJ.*, 399(2):656-664, 1992.

[22] Maria Goeppert Mayer and J. Hans Jensen Elementary Theory of Nuclear Shell Structure John Wiley and Sons, New York, 1955.

[23] R.F. Casten Nuclear Structure From a Simple Perspective Oxford University Press, New York, 2000.

[24] A. Navin et al. *Phys. Rev. Lett.*, 85:266, 2000.

[25] B. Pfeiffer, K.-L. Kratz, F.-K. Thielemann, *Z. Phys.*, A357:235, 1997.

[26] K. Farouqi et al. Astrophysical conditions for an r-process in the high-entropy wind scenario of type II supernovae. *Nucl. Phys. A*, 758:631-634, 2005.

[27] I. Dillmann et al. *Phys.Rev.Lett.*, 91:162503, 2003.

[28] K. Heyde *Nucl. Phys. A*, 507:149-154, 1990.

[29] K.S. Krane Introductory Nuclear Physics Wiley, New York, 1988.

[30] R.F. Casten *Nucl. Phys. A*, 443:1-28, 1985.

[31] P. Federman and S. Pittel *Phys. Rev. C*, 20:820, 1979.

[32] A. Aprahamian et al. *Phys. Lett.*, 140B:22, 1984.

[33] U.C. Bergmann et al. *Nucl. Phys. A*, 714:21, 2003.

[34] CF Von Weizscker Theory of Nuclear Masses *Z. Phys.*, 1935.

[35] H. Bethe and R. Bacher Stationary States of Nuclei *Rev. Mod. Phys.*, 8:165, 1936.

[36] W.D.Myers and W.J.Swiatecki Nuclear Masses and Deformations *Nucl. Phys.*, 81:1, 1966.

[37] D. Lunney, J.M. Pearson, and C. Thibault Recent Trends in the Determination of Nuclear Masses *Rev. Mod. Phys.*, 75, 2003.

[38] P. Moller et al. Nuclear Ground-State Masses and Deformations *ADNDT*, 59:185, 1995.

[39] A.K. Dutta et al. *Nucl. Phys. A*, 458:77,1986.

[40] J.M. Pearson and S. Goriely Nuclear Mass Formulas for Astrophysics *Nucl. Phys. A*, 777:623,2006.

[41] A. Aprahamian et al. *Hyperfine Interactions*, 132:417424, 2001.

[42] T. Takahashi, M. Yamada and T. Kondoh *ADNDT*, 12:101,1973.

[43] J. Halbleib and R. Sorensen *Nucl. Phys. A*, 98:542,1967.

[44] P. Moller, J.R. Nix, and K.L.Kratz *ADNDT*, 66:131, 1997.

[45] J. Skalski, S. Mizutori and W. Nazarewicz *Nuclear Physics A*, 617:282, 1997.

[46] R.V.F. Janssens et al. *Phys. Lett. B*, 546:55, 2002.

[47] P.T. Hosmer et al. *Phys. Rev. Lett.*, 94:112501, 2005.

[48] A1900 *Nucl. Instrum. Meth. B*, 204:90, 2003.

[49] J.I. Prisciandaro, A.C. Morton and P.F. Mantica *Nucl. Instrum. Meth. A*, 505:140, 2002.

[50] B.Pfeiffer, K.L. Kratz, and P.Moller Status of delayed neutron precursor data: half-lives and neutron emission probabilities *Prog. Nucl. Energy*, 41:39-69, 2002.

Cowan J.J. Cowan, F.K. Thielemann, and J.W. Truran *Physics Reports*, 208:267, 1991.